Drift-cyclotron loss-cone instability in 3-D simulations of a sloshing-ion simple mirror

Tran, Aaron; Frank, Samuel; Le, Ari Yitzchak; Stanier, Adam John; Wetherton, Blake Alastair; Egedal, Jan; Endrizzi, Doug; Harvey, Robert; Petrov, Yuri; Qian, Tony; Sanwalka, Kunal; Viola, Jesse; Forest, Cary; Zweibel, Ellen

To be published in: Journal of Plasma Physics

DOI to publisher's version: 10.1017/S0022377825000480

J. Plasma Phys. (2025), *vol*. 91, E85
 doi:10.1017/S0022377825000480

Drift-cyclotron loss-cone instability in 3-D simulations of a sloshing-ion simple mirror

Aaron Tran[1], Samuel J. Frank[2], Ari Y. Le[3], Adam J. Stanier[3], Blake A. Wetherton[3], Jan Egedal[1], Douglass A. Endrizzi[2], Robert W. Harvey[4], Yuri V. Petrov[4], Tony M. Qian[1,5], Kunal Sanwalka[1], Jesse Viola[2], Cary B. Forest[1,2] and Ellen G. Zweibel[1,6]

[1]Department of Physics, University of Wisconsin–Madison, Madison, WI, USA
[2]Realta Fusion, Madison, WI, USA
[3]Los Alamos National Laboratory, Los Alamos, NM, USA
[4]CompX, Del Mar, CA, USA
[5]Princeton Plasma Physics Laboratory, Princeton, NJ, USA
[6]Department of Astronomy, University of Wisconsin–Madison, Madison, WI, USA

Corresponding author: Aaron Tran, atran@physics.wisc.edu

(Received 4 December 2024; revision received 14 April 2025; accepted 16 April 2025)

The kinetic stability of collisionless, sloshing beam-ion (45° pitch angle) plasma is studied in a three-dimensional (3-D) simple magnetic mirror, mimicking the Wisconsin high-temperature superconductor axisymmetric mirror experiment. The collisional Fokker–Planck code CQL3D-m provides a slowing-down beam-ion distribution to initialize the kinetic-ion/fluid-electron code Hybrid-VPIC, which then simulates free plasma decay without external heating or fuelling. Over 1–10 μs, drift-cyclotron loss-cone (DCLC) modes grow and saturate in amplitude. The DCLC scatters ions to a marginally stable distribution with gas-dynamic rather than classical-mirror confinement. Sloshing ions can trap cool (low-energy) ions in an electrostatic potential well to stabilize DCLC, but DCLC itself does not scatter sloshing beam-ions into the said well. Instead, cool ions must come from external sources such as charge-exchange collisions with a low-density neutral population. Manually adding cool ∼1 keV ions improves beam-ion confinement several-fold in Hybrid-VPIC simulations, which qualitatively corroborates prior measurements from real mirror devices with sloshing ions.

Keywords: Plasma Simulation, Plasma Instabilities, Plasma Devices

1. Introduction

The Wisconsin high-temperature superconductor axisymmetric mirror (WHAM) is a new laboratory experiment that confines hot plasmas in a magnetic mirror

with a maximum field of 17 T on axis, generated by high-temperature superconductors (HTS) (Endrizzi *et al.* 2023). For WHAM and future mirror devices (Simonen *et al.* 2008; Bagryansky 2024; Forest *et al.* 2024) to succeed, both fluid and kinetic plasma instabilities must be quelled.

A kinetic instability of particular concern is the drift-cyclotron loss-cone (DCLC) instability (Post & Rosenbluth 1966; Baldwin 1977). The DCLC comprises a spectrum of ion Bernstein waves, coupled to a collisionless drift wave, which is excited by a spatial density gradient ∇n and a loss-cone ion velocity distribution. In a magnetized plasma column, DCLC appears as an electrostatic wave that propagates around the column's azimuth in the ion diamagnetic drift direction, perpendicular to both $\boldsymbol{B}$ and ∇n. The DCLC can be unstable solely due to ∇n when the gradient length scale $n/(\nabla n)$ is of the order of the ion Larmor radius ρ_i, even for distributions without a loss cone (e.g. Maxwellians), in which case it may be called a drift-cyclotron instability (Mikhailovskii & Timofeev 1963). In this manuscript, we call both drift-cyclotron and drift-cyclotron loss-cone modes by the acronym 'DCLC' for simplicity.

Many mirror devices have measured electric and/or magnetic fluctuations at discrete ion cyclotron harmonics having properties consistent with DCLC. These devices include PR-6 (Bajborodov *et al.* 1971; Ioffe *et al.* 1975), PR-8 (Piterskiĭ *et al.* 1995), 2XIIB (Coensgen *et al.* 1975), TMX and TMX-U (Drake *et al.* 1981; Simonen *et al.* 1983; Berzins & Casper 1987), LAMEX (Ferron & Wong 1984), MIX-1 (Koepke *et al.* 1986*a*, *b*; McCarrick *et al.* 1987; Burkhart *et al.* 1989), GAMMA-6A (Yamaguchi 1996) and the gas dynamic trap (GDT) (Prikhodko *et al.* 2018; Shmigelsky *et al.* 2024). Experiments on these devices showed that DCLC may be partly or wholly stabilized by filling the ions' velocity-space loss cone via axial plasma stream injection (Ioffe *et al.* 1975; Coensgen *et al.* 1975; Kanaev 1979; Correll *et al.* 1980; Drake *et al.* 1981; Simonen *et al.* 1983; Berzins & Casper 1987), filling the loss cone via angled neutral beam injection, which creates a non-monotonic axial potential that traps cool ions (Kesner 1973, 1980; Fowler *et al.* 2017; Shmigelsky *et al.* 2024), decreasing ∇n with respect to the ion Larmor radius ρ_i (Ferron & Wong 1984) and bounce-resonant electron Landau damping (Koepke *et al.* 1986*a*). Other effects theoretically calculated to modify and/or help stabilize DCLC include finite plasma beta (Tang *et al.* 1972), radial ambipolar electric fields (Chaudhry 1983; Sanuki & Ferraro 1986) and low-frequency external electric fields (Aamodt 1977; Hasegawa 1978).

The WHAM plasma column is a few to several ion Larmor radii (ρ_i) in width and so may excite DCLC. How will DCLC appear in WHAM; i.e. what will be its azimuthal mode number, oscillation frequency and amplitude? Sloshing ions, injected at 45° pitch-angle, helped to suppress DCLC in TMX-U endplugs and are also used on WHAM; to what extent can sloshing ions similarly suppress DCLC in WHAM? In general, how should WHAM's plasma properties be tuned to suppress DCLC? These questions have been addressed to varying degrees, for previous devices, via linear theory (Post & Rosenbluth 1966; Tang *et al.* 1972; Gerver 1976; Lindgren *et al.* 1976; Baldwin 1977; Cohen *et al.* 1982, 1983; Ferraro *et al.* 1987; Kotelnikov *et al.* 2017; Kotelnikov & Chernoshtanov 2018), quasilinear theory (Baldwin *et al.* 1976; Berk & Stewart 1977), nonlinear theory (Aamodt 1977; Aamodt *et al.* 1977; Myer & Simon 1980) and one- and two-dimensional (2-D) kinetic computer simulations (Cohen & Maron 1980; Aamodt *et al.* 1981; Cohen *et al.* 1982, 1983, 1984; Rose *et al.* 2006).

https://doi.org/10.1017/S0022377825000480 Published online by Cambridge University Press

Here, we address the aforementioned questions using 3-D full-device computer simulations of DCLC growth and saturation in a hybrid (kinetic ion, fluid electron) plasma model. Our simulation accounts for many physical effects relevant to WHAM – magnetic geometry, beam-ion distributions, both radial and axial electrostatic potentials and diamagnetic field response – to obtain a fuller and more integrated kinetic model than was possible decades ago. We highlight that the initial beam-ion distributions are obtained from a Fokker–Planck collisional-transport model of a WHAM shot's full 20 ms duration. The Fokker–Planck modelling and code-coupling methods are presented by a companion study, Frank *et al.* (2025) within this journal issue.

In § 2 we describe our simulation methods and parameters. In §§ 3.1 to 3.3, we characterize three fiducial simulations evolved to 6 μs that have reached a steady-state decay. The main instability in all simulations is described and identified as DCLC, with the aid of an approximate linear dispersion relation for electrostatic waves in an inhomogeneous, low-β planar-slab plasma. In § 3.4, particle confinement is shown to obey a 'gas dynamic' rather than 'collisionless mirror' scaling with mirror ratio and device length. In §§ 4.1–4.3, we survey well-known ways to stabilize DCLC that may be relevant to WHAM and next-step mirror devices. We particularly focus on stabilization via trapped cool ions, and we show that adding cool ions can improve beam-ion confinement several-fold in our simulations. In §§ 4.4 and 4.5 we briefly discuss how DCLC in WHAM fits into a broader landscape of other instabilities and devices. Finally, § 5 concludes.

2. Methods

2.1. *Simulation overview*

We simulate freely decaying plasma in a three-dimensional (3-D) magnetic mirror made of one central cell and two expanders (figure 1*a,e,i*). Three magnetic-field configurations are used, labelled by the vacuum mirror ratio $R_m = \{20, 41, 64\}$, to span WHAM's operating range. The WHAM magnetic field is created by two HTS coils at $z = \pm 98$ cm and two copper coils at $z = \pm 20$ cm (Endrizzi *et al.* 2023). When both HTS and copper coils are fully powered, the magnetic field on axis varies between $B \approx 17.3$ T at the mirror throats to 0.86 T at the device's centre ($R_m = 20$). When the copper coils are partly powered, B on axis ranges between 17.2 to 0.414 T ($R_m = 41$). When the copper coils are unpowered, B on axis ranges between 17.1 to 0.267 T ($R_m = 64$).

Our simulations are performed with the code Hybrid-VPIC[1] (Le *et al.* 2023; Bowers *et al.* 2008), which models ion kinetics using the particle-in-cell (PIC) method and models electrons as a neutralizing fluid. Ions are advanced using a Boris pusher (Bowers *et al.* 2008). Electric and magnetic fields $\boldsymbol{E}$, $\boldsymbol{B}$ are evolved on a rectilinear Cartesian (x, y, z) mesh. Particle–mesh interpolation uses a quadratic-sum shape (Le *et al.* 2023; Appendix B); no filtering of the deposited particle charge and currents is applied. The magnetic field is advanced using Faraday's Law, $\partial \boldsymbol{B}/\partial t = -c\nabla \times \boldsymbol{E}$, with a fourth-order Runge–Kutta scheme. The electric field is passively set by a generalized Ohm's law without electron inertia,

$$\boldsymbol{E} = -\frac{\boldsymbol{V}_i \times \boldsymbol{B}}{c} + \frac{\boldsymbol{j} \times \boldsymbol{B}}{en_e c} - \frac{\nabla P_e}{en_e} + \eta \boldsymbol{j} - \eta_H \nabla^2 \boldsymbol{j}, \tag{2.1}$$

[1] Publicly available at https://github.com/lanl/vpic-kokkos/tree/hybridVPIC.

https://doi.org/10.1017/S0022377825000480 Published online by Cambridge University Press

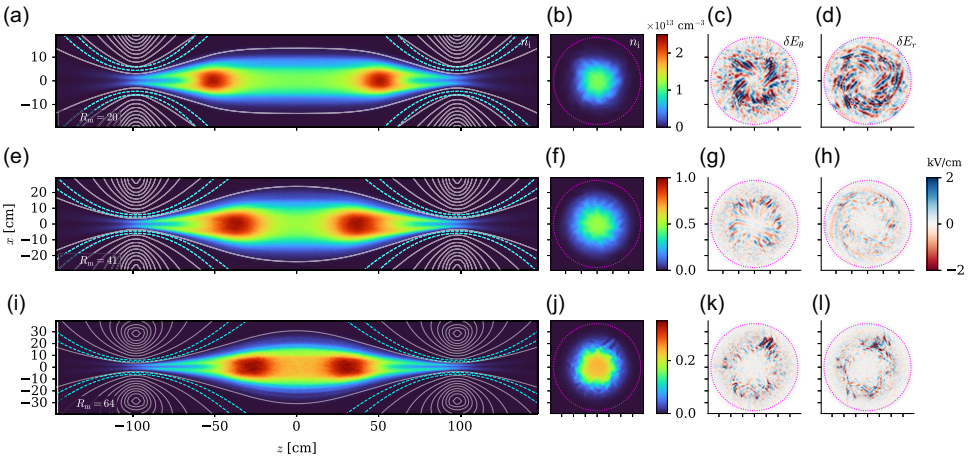

FIGURE 1. The 2-D images of ion density and electric field fluctuations at $t \approx 6\tau_{\text{bounce}} \approx 6\mu s$, for three simulations with varying vacuum mirror ratio (*a–d*) $R_m = 20$, (*e–h*) 41, (*i–l*) 64. (*a*) Ion density n_i in units of $10^{13}\,\text{cm}^{-3}$, 2-D slice at $y = 0$ in (x, y, z) coordinates. White lines trace vacuum magnetic fields; dashed cyan lines trace hyper-resistive dampers and conducting $E = 0$ regions (see text). (*b*) Like (*a*), but 2-D slice at the mirror's midplane $z = 0$ showing coherent flute-like fluctuations at the plasma edge. (*c*) Azimuthal electric field fluctuation δE_θ in $\text{kV}\,\text{cm}^{-1}$; magenta dotted line traces radial conducting boundary. (*d*) Like (*c*), but radial fluctuation δE_r. Panels (*e*)–(*h*) and (*i*)–(*l*) are organized like panels (*a*)–(*d*). Aspect ratio is distorted in panels (*a*), (*e*) and (*i*); aspect ratio is to scale in all other panels. The ion bounce time τ_{bounce} is defined later in § 2.3.

assuming both $\boldsymbol{j} = c\nabla \times \boldsymbol{B}/(4\pi)$ and $n_e = n_i$. We further take $P_e = n_e T_e$, with T_e constant in time and space (isothermal). Here n_i and n_e are ion and electron number densities, $\boldsymbol{V}_i$ is bulk ion velocity, P_e is scalar electron pressure, $\boldsymbol{j}$ is current density, η is resistivity, η_H is hyper-resistivity, c is the speed of light and e is the elementary charge. Gaussian CGS units are used in this manuscript unless otherwise stated.

Coulomb collisions are neglected because the ion–ion deflection and ion–electron drag time scales in the plasmas modeled here are of order $O(\text{ms})$, longer than our simulation durations $\sim$1–10 μs.

The hybrid-PIC equations solved here are non-relativistic: the displacement current $\partial \boldsymbol{E}/\partial t/(4\pi)$ is omitted from Ampére's law, and no Lorentz factors are used in the Boris push. The speed of light is effectively infinite. All code equations are solved in a dimensionless form; the normalizations for converting code variables into physical units are set by choosing reference values of density, magnetic field, and ion species' mass and charge.

A density floor of $n_e \geqslant \{15, 6, 1.5\} \times 10^{11}\,\text{cm}^{-3}$, for the $R_m = \{20, 41, 64\}$ simulations, respectively, is applied in the Hall and ambipolar (pressure gradient) terms of (2.1) to prevent division-by-zero in vacuum and low-density regions surrounding the plasma. The density floor is set low enough to obtain the electrostatic potential drop from $z = 0$ out to the mirror throats at $z = \pm 98$ cm, but the remaining potential drop from throat into expanders is not captured. Lowering the density floor increases compute cost, so we sacrifice physics in the expanders that is less-accurately described by the hybrid-PIC model anyways.

The simulation time step Δt must be smaller than a Courant–Friedrichs–Lewy (CFL) limit to resolve gridscale whistler waves: $\Delta t \propto n(\Delta z)^2/B$ for cell size Δz

https://doi.org/10.1017/S0022377825000480 Published online by Cambridge University Press

less than the ion skin depth. The density floor in high-$\boldsymbol{B}$ vacuum regions thus sets the overall simulation time step. The CFL-limited time step is well below the ion-cyclotron period and other physical time scales of interest, so we subcycle the magnetic-field update $N_{\rm sub}$ times within each particle push to reduce compute cost. The CFL limit then applies to $\Delta t/N_{\rm sub}$, and larger Δt can be used.

We set the resistivity $\eta = 0$ and the hyper-resistivity $\eta_H = 2.75 \times 10^{-14}\,\mathrm{s\,cm^2}$. Hyper-resistivity is used solely to damp high-frequency whistler noise at the grid scale $k \sim \pi/\Delta z$; η_H does not represent any subgrid physics of interest to us. The hyper-resistive $\boldsymbol{E}$ is included in the ion push, since it is not used to model electron–ion friction.[2] Hyper-resistivity is the only explicit form of numerical dissipation in our simulations

2.2. *Simulation geometry*

The simulation domain for the $R_m = 20$ case is a rectangular box with extent $L_x = L_y = 39.2\,\mathrm{cm}$ and $L_z = 294\,\mathrm{cm}$. The box is decomposed into a $96^2 \times 384$ Cartesian (x, y, z) mesh with cell dimensions $\Delta x = \Delta y = 0.41\,\mathrm{cm}$ and $\Delta z = 0.77\,\mathrm{cm}$. For analysis and discussion, we project data into usual cylindrical coordinates (r, θ, z). For the $R_m = 41$ and 64 cases, the domain is enlarged to $L_x = L_y = 58.8$ and 78.4 cm respectively while preserving the mesh cell shape, so the number of mesh points is $144^2 \times 384$ and $192^2 \times 384$, respectively. The domain extent truncates the expanders at $z = \pm 147\,\mathrm{cm}$, unlike the real experiment, wherein a set of staggered biasable rings collects escaping plasma at $z \sim 190$–$210\,\mathrm{cm}$ (Endrizzi *et al.* 2023; Qian *et al.* 2023).

The overall simulation time step $\Delta t = 7.3 \times 10^{-11}\,\mathrm{s}$. The magnetic-field advance is subcycled $N_{\rm sub} = \{100, 250, 1000\}$ times within Δt, for $R_m = \{20, 41, 64\}$, respectively.

Hyper-resistivity η_H acts like smoothing and removes gridscale numerical noise on the whistler-wave dispersion branch, which would otherwise be undamped in the absence of resistivity or hyper-resistivity. The value of η_H must be kept small enough to not artificially smooth real physical phenomena. The hyper-resistive diffusion time scale estimated as $\left[\eta_H c^2/(4\pi L^4)\right]^{-1}$ for an arbitrary length scale L is $1.4 \times 10^{-8}\,\mathrm{s}$ for the transverse grid scale $L \sim \Delta x$; it is 600 μs for the ion skin depth $L \sim c/\omega_{\rm pi} \sim 6\,\mathrm{cm}$ with $n \sim 3 \times 10^{13}\,\mathrm{cm^{-3}}$. We cannot make η_H much larger because the scale separation between grid noise and physical phenomena is small; high-m kinetic modes lie below the ion skin depth. In Appendix A, we present density fluctuation properties from a three-point scan of η_H; some details (e.g. spectral bandwidth) are altered, but the main conclusions regarding DCLC are not too sensitive to our chosen value of η_H.

Particle and field boundary conditions are imposed as follows. A conducting radial sidewall is placed at $r = 0.47 L_x$, which is in physical units $\{18.4, 27.6, 36.8\}\,\mathrm{cm}$ for $R_m = \{20, 41, 64\}$, respectively. A conducting axial sidewall is placed at $z = 0.485 L_z = \pm 143\,\mathrm{cm}$. The HTS coils are also surrounded by both conducting and hyper-resistive wrapper layers (figure 1*a,e,i*, dashed cyan curves). Within the wrapper layer (between nested dashed cyan curves), the grid-local value of η_H used in Ohm's law (2.1) is increased 30× to help suppress numerical noise in high-field, low-density regions. The 'conducting' boundary is enforced by setting $\boldsymbol{E} = 0$ on the

[2]If hyper-resistivity were used to model electron–ion friction, and no explicit collision operator for ions is used, only the frictionless $\boldsymbol{E}$ should be used in the ion push (Stanier *et al.* 2019, Appendix A).

https://doi.org/10.1017/S0022377825000480 Published online by Cambridge University Press

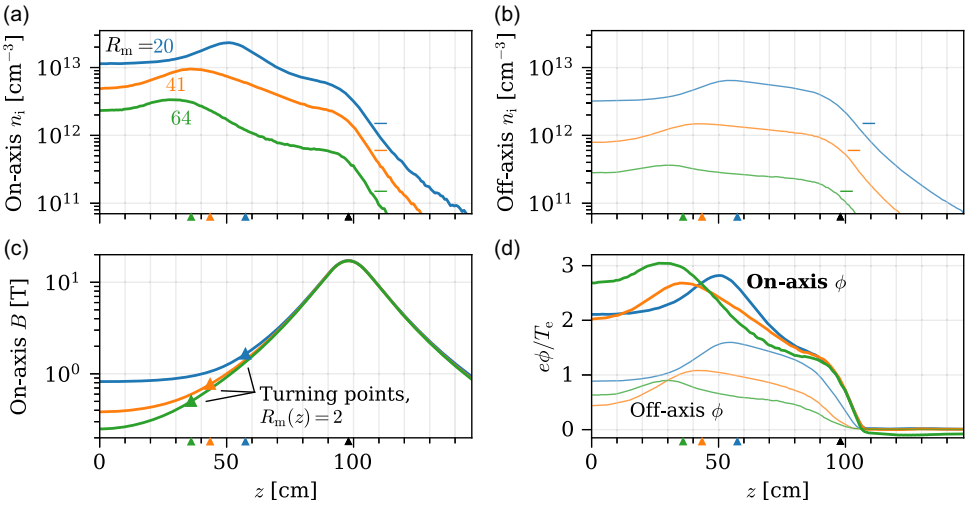

FIGURE 2. Axial profiles of n_i, B, ϕ measured at $t = 6\tau_{\text{bounce}} \approx 6\mu$s. (*a*) Ion density n_i on axis ($r = 0$). Dashes mark density floor for Ohm's law, (2.1). (*b*) Like (*a*), but measured along off-axis flux surfaces. (*c*) Magnetic-field strength B on axis. Ions with 45° pitch angle turn where the local mirror ratio $R_m(z) = 2$ (triangles). (*d*) Electrostatic potential $e\phi$ in units of electron temperature T_e, measured on-axis (thick curves) and off-axis (thin curves). Potentials truncate at $z \sim 100$ cm, corresponding to density floors marked in (*a*) and (*b*). In all panels: blue, orange, green curves are simulations with vacuum $R_m = \{20, 41, 64\}$, respectively; small triangles mark on-axis turning points $R_m(z) = 2$ (coloured) and mirror throat (black).

mesh, which disables $\boldsymbol{B}$ field evolution. Bound charge and image currents within conducting surfaces are not explicitly modelled. Particles crossing the Cartesian domain boundaries ($x = \pm L_x/2$, $y = \pm L_y/2$, $z = \pm L_z/2$) are removed from the simulation. Boundary conditions are applied to $\boldsymbol{E}$ at cell centres in a nearest-gridpoint manner, which may contribute to mesh imprinting; boundaries might be improved with a cut-cell algorithm or simply higher grid resolution in future work.

2.3. *Plasma parameters*

We model a fully ionized deuteron–electron plasma ($m_i = 3.34 \times 10^{-24}$ g) with typical ion density $n_i \sim 10^{12}$ to 10^{13} cm^{-3} and temperature $T_i \sim 5$ to 13 keV in the mirror's central cell. The ion velocity distribution is a beam slowing-down distribution with pitch angle $\cos^{-1}(v_\parallel/v) \sim 45°$ at the mirror midplane ($z = 0$) to mimic WHAM's angled neutral beam injection (NBI). The beam path is centred on axis ($r = 0$).

The ions' spatial and velocity distributions are obtained from the bounce-averaged, zero-orbit-width, collisional Fokker–Planck code CQL3D-m (Petrov & Harvey 2016; Forest *et al.* 2024). We initialize the CQL3D-m simulations with a 1.5×10^{13} cm^{-3} plasma at low temperature $T_i = T_e = 250$ eV, mimicking the initial electron-cyclotron heating (ECH) breakdown of a gas puff in WHAM.[3] The plasma is simulated

[3]The 250 eV temperature is higher than in experiments so that we can use coarser velocity-space grid resolution. The final evolved solution varies little with initial temperature.

https://doi.org/10.1017/S0022377825000480 Published online by Cambridge University Press

by CQL3D-m on 32 flux surfaces spanning normalized square root poloidal flux, $\sqrt{\psi_n} = 0.01$–0.9, as it is fuelled and heated with a realistic 25 keV neutral beam operating at the experimental parameters. No heating or fuelling sources other than the neutral beam are included. The velocity-space grid has 300 points in total momentum-per-rest-mass $p/(mc)$, and either 256 or 300 points in pitch angle. The total-momentum grid is not linearly spaced, but instead geometrically scaled at low energies to cover the ion distribution function. The pitch-angle grid is uniformly spaced. The solver CQL3D-m uses a time step of 0.0625 ms, advancing ions and electrons simultaneously. The neutral beam deposition profile is updated after each time step using the CQL3D-m internal FREYA neutral-beam Monte Carlo solver. To include the diamagnetic $\boldsymbol{B}$-field response to the plasma pressure, the CQL3D-m solver is iterated with the MHD equilibrium solver Pleiades[4] (Peterson 2019), with improvements to treat pressure-anisotropic equilibria (Frank *et al.* 2025). The CQL3D-m and Pleiades solvers are coupled using a customized version of the integrated plasma simulator framework (Elwasif *et al.* 2010). The diamagnetic field is updated in CQL3D-m every 1 ms.

We perform separate CQL3D-m runs for each of the $R_m = \{20, 41, 64\}$ cases. In each case, the NBI power is adjusted in 100 kW increments, until the 1 MW maximum input power of the experiment is reached or a mirror instability driven β limit occurs (Kotelnikov 2025). The $R_m = \{20, 41, 64\}$ cases operate with NBI power $\{200, 400, 1000\}$ kW, respectively. The CQL3D-m/Pleiades loop is run for the duration of a laboratory shot, to 20 ms (which is $t = 0$ for Hybrid-VPIC). At the end of the CQL3D-m run, all three cases have plasma $\beta \sim 0.60$. The low $R_m = 20$ (high $\boldsymbol{B}$-field) case achieves the highest plasma density 1–3×10^{13} cm^{-3} on axis in the central cell (figure 2*a*). The ions have $T_i = \{13, 11, 11\}$ keV at the origin $(r, z) = (0, 0)$ in the $R_m = \{20, 41, 64\}$ cases, respectively. Of note, the $R_m = 64$ case has a cooler ion plasma temperature $T_i \sim 5$ keV at the plasma's radial edge, whereas the lower R_m (higher field) CQL3D-m simulations maintain $T_i \sim 10$ keV from the axis $r = 0$ to the edge. This is a result of the larger cool thermal ion population that is trapped by the sloshing-ion distribution in the $R_m = 64$ case.

The CQL3D-m bounce-averaged distribution function at the mirror's midplane ($z = 0$) is mapped on Liouville characteristics to all (r, z) and read into Hybrid-VPIC as an initial condition for both real- and velocity-space ion distributions. The CQL3D-m ion radial density profile n is extrapolated from $\sqrt{\psi_n} = 0.9$ to 1 as

$$n(\psi_n) = \cos^2\left[\frac{\pi}{2}\left(\frac{\psi_n - 0.81}{1 - 0.81}\right)\right], \tag{2.2}$$

where $\psi_n = \psi/\psi_{\text{limiter}}$, $\psi = \int 2\pi B r \mathrm{d}r$ and $\psi_{\text{limiter}} = 2.32 \times 10^6$ G cm^2. This sets the plasma's initial extent. No limiter boundary condition is implemented in the Hybrid-VPIC simulation.

Electron velocity distributions and the electrostatic potential ϕ are also solved in CQL3D-m via an iterative technique (Frank *et al.,* 2025) but neither are directly input to Hybrid-VPIC's more-approximate fluid electron model. Instead, we set the Hybrid-VPIC electron temperature $T_e = \{1.25, 1.5, 1.0\}$ keV in the $R_m = \{20, 41, 64\}$ cases, respectively, with T_e values taken from the CQL3D-m simulation at

[4] https://github.com/eepeterson/pleiades

https://doi.org/10.1017/S0022377825000480 Published online by Cambridge University Press

R_m	L_p	$B(z=0)$	f_ci0	v_ti0	ρ_i0	T_e	Core T_i at 0 μs	Edge $T_{i\perp}$ at 6 μs	Edge $T_{i\parallel}$ at 6 μs
20	98 cm	0.86 T	6.5 MHz	980 km s^{-1}	2.37 cm	1.25 keV	13 keV	8.4 keV	17.1 keV
41	···	0.41	3.1	···	4.94	1.5	11	6.5	13.1
64	···	0.27	2.0	···	7.64	1.0	11	6.4	8.0

TABLE 1. Physical parameters for fiducial simulations, labelled by vacuum mirror ratio R_m. The ion cyclotron frequency $f_\mathrm{ci0} = \Omega_\mathrm{i0}/(2\pi)$ and ion Larmor radius $\rho_\mathrm{i0} = v_\mathrm{ti0}/\Omega_\mathrm{i0}$. Ions are deuterons. Core T_i at 0 μs is measured at the origin $(r, z) = (0, 0)$.

$(r, z) = (0, 0)$. All simulations use an isothermal equation of state, so T_e is constant in space and time. To support our use of a fluid approximation, we note that the electron–electron collision time is much shorter than a WHAM shot duration, so the CQL3D-m electron distributions are Maxwellians with empty loss-cones beyond $v_\parallel \sim \sqrt{e\phi/m_e}$ (since the axial ambipolar potential confines 'core' thermal electrons). The overall T_e varies by less than $2\times$ in both axial and radial directions, within sloshing ion turning points, in the $R_m = 20$ case.

We use $N_\mathrm{ppc} = 8000$ ion macroparticles per cell, pinned to a reference density 3×10^{13} cm^{-3}, so the initial number of particles is highest at the beam-ion turning points and lower elsewhere; all particles have equal weight in the PIC algorithm.

We initialize particles on their gyro-orbits with random gyrophase; this spatially smooths the initial radial distribution of plasma density and pressure, as compared with the CQL3D-m density distribution which places particles at their gyrocentres. The initial plasma in Hybrid-VPIC thus has non-zero initial azimuthal diamagnetic drift and hence net angular momentum. We also initialize the diamagnetic field from Pleiades in the Hybrid-VPIC simulation, but our initial plasma and magnetic pressures are not in equilibrium due to the Larmor radius offsets from particle gyrocentres. Thus, the Hybrid-VPIC simulation evolves towards a new pressure equilibrium as the plasma settles into steady state.

Finally, the initial electric field $\boldsymbol{E}(t=0)$ in Hybrid-VPIC is given by (2.1) combined with the initial ion distributions from CQL3D-m, our chosen values of T_e, and the summed vacuum and diamagnetic $\boldsymbol{B}$ fields from Pleiades.

Let us define thermal length and time normalizations. The angular ion cyclotron frequency $\Omega_\mathrm{i0} = eB(z=0)/(m_i c)$ at the mirror midplane. The ion bounce (or, axial-crossing) time $\tau_\mathrm{bounce} = L_\mathrm{p}/v_\mathrm{ti0} \approx 1$ μs using the mirror's half-length $L_\mathrm{p} = 98$ cm and a reference ion thermal velocity $v_\mathrm{ti0} = \sqrt{T_\mathrm{i0}/m_i} = 0.00327c = 9.8 \times 10^7$ cm s^{-1}, with $T_\mathrm{i0} = 20$ keV and c the speed of light. Though the CQL3D-m initialized ions have $T_i \sim 10$ keV, our chosen v_ti0 approximates $m_i v_\mathrm{ti0}^2/2 \sim m_i v_\perp^2/2 \sim m_i v_\parallel^2/2 \sim (25\,\mathrm{keV})/2$ for the beam-ion distribution's primary and secondary peaks. We also define a reference ion Larmor radius $\rho_\mathrm{i0} = v_\mathrm{ti0}/\Omega_\mathrm{i0}$ at the mirror midplane. Tables 1 and 2 summarize physical and numerical parameters, respectively, for our three fiducial simulations.

https://doi.org/10.1017/S0022377825000480 Published online by Cambridge University Press

R_m	L_x	L_z	Δx	Δz	Δt	$N_{\rm sub}$	η	η_H
20	39.2 cm	294 cm	0.41 cm	0.77 cm	7.3×10^{-11} s	100	0 s	2.75×10^{-14} s cm^2
41	58.8	···	···	···	···	250	···	···
64	78.4	···	···	···	···	1000	···	···

TABLE 2. Numerical parameters for fiducial simulations, labelled by vacuum mirror ratio R_m.

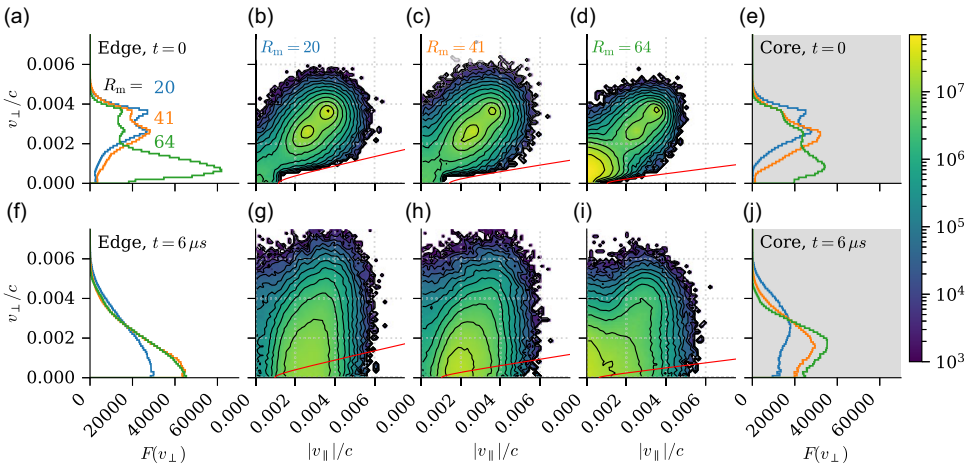

FIGURE 3. (*a–e*) Initial and (*f–j*) relaxed ion velocity distributions at the plasma edge, in three simulations. Edge ion distributions smooth and flatten in $v_\perp$ as the simulation evolves, with a stronger effect for edge plasma as compared with core plasma. The loss cone is filled, and the distribution varies little across the loss-cone boundary. (*a*) Reduced distribution $F(v_\perp)$ for simulations with vacuum $R_m = 20$ (blue), 41 (orange) and 64 (green). Distribution is normalized so that $\int F(v_\perp) 2\pi v_\perp \mathrm{d}v_\perp = 1$. (*b*)–(*d*) The 2-D distributions $f(v_\perp, v_\parallel)$ for each of the three simulations shown in (*a*), normalized so that $\int f 2\pi v_\perp \mathrm{d}v_\perp \mathrm{d}v_\parallel = 1$. Red curves plot loss-cone boundary, with the effect of electrostatic trapping approximated using the on-axis potential well depth of 0.4 to 1.9 keV. (*e*) Like (a), but a 'core' distribution centred on $r = 0$ for comparison with the 'edge'. (*f*)–(*j*) Like (*a–e*), but at later time $t = 6\mu s$ in the simulation. In all panels, velocities $v_\perp$, $v_\parallel$ are normalized to the speed of light c.

3. Results

3.1. *Space, velocity structure of steady-state decay*

At the start of each simulation, the plasma relaxes from its initial state over ∼1–$3\tau_{\rm bounce}$; the diamagnetic field response is changed, short-wavelength electrostatic fluctuations occur at the plasma edge and plasma escapes from the central cell into the expanders. The plasma reaches a steady-state decay by $t = 6\tau_{\rm bounce}$ for all R_m simulations. At this time: (i) the particle loss time $\tau_{\rm p} = n/(\mathrm{d}n/\mathrm{d}t)$ is roughly constant and exceeds the ion bounce time ($\tau_{\rm p} \gg \tau_{\rm bounce}$); (ii) the plasma beta $\beta_i = 8\pi P_i/B^2 \sim 0.1$ to within a factor of two at the origin $(r, z) = (0, 0)$, with P_i the total ion pressure; (iii) the combined vacuum and diamagnetic fields attain a mirror ratio $R_m = \{21, 45, 69\}$ somewhat higher than the respective vacuum values $R_m = \{20, 41, 64\}$.

https://doi.org/10.1017/S0022377825000480 Published online by Cambridge University Press

Figure 1 shows the plasma's overall structure at $t = 6\tau_{\text{bounce}}$ for each of the vacuum $R_m = 20, 41, 64$ simulations. Flute-like, electrostatic fluctuations at the plasma's radial edge are visible in $z = 0$ slices of ion density and electric fields, with the strongest and most coherent fluctuations for the $R_m = 20$ case. In figure 1(*a,e,i*), the axial outflow at $|z| \gtrsim 70$ cm is split about $r = 0$, so more plasma escapes from the radial edge $r > 0$ than the core $r \sim 0$. In figure 1(*d,h,l*), the radial electric field fluctuation $\delta E_r = E_r - \langle E_r \rangle_\theta$, where $\langle \cdots \rangle_\theta$ represents an average over the azimuthal coordinate to subtract the plasma's net radial potential. The azimuthal fluctuation δE_θ in figure 1(*c,g,k*) is defined similarly. The transverse magnetic fluctuations δB_r and δB_θ have small amplitudes $\lesssim 10^{-3} B(z = 0)$, whereas the electric fluctuations δE_r and δE_θ are of order $0.1 v_{\text{ti}0} B(z = 0)/c$, corresponding to motional flows at thermal speeds. We therefore neglect electromagnetic fluctuations and focus solely on the azimuthal, electrostatic mode visible in figure 1.

Figure 2(*a,b*) shows ion density profiles along z both on- and off-axis, with horizontal dashes marking the density floor imposed in Ohm's law, (2.1). The off-axis density is measured along flux surfaces hosting the strong electric fluctuations seen in figure 1. Specifically, we pick surfaces at $r = \{9, 18, 22\}$ cm and $z = 0$ that have an approximate (azimuth-averaged, paraxial) flux coordinate $\psi \approx \int 2\pi \langle B_z \rangle_\theta r \mathrm{d}r = \{2.1, 3.8, 3.7\} \times 10^6\ \mathrm{G\,cm^2}$ for the $R_m = \{20, 41, 64\}$ simulations, respectively. The plotted density n_i is also azimuth averaged.

The density profiles peak near the turning points of 45° pitch-angle ions, defined as the z locations where the local mirror ratio $R_m(z) = 2$ on axis; i.e. {57, 44, 36} cm (figure 2*c*). Comparing on- and off-axis density peaks, the off-axis peak is wider and decreases more slowly towards the mirror throat and expander. This can be explained by the plasma edge's stronger loss-cone outflow and broader pitch-angle distribution between 0° and 45°, compared with the plasma core at $r = 0$ (figure 3).

Figure 2(*d*) shows on- and off-axis electrostatic potential profiles $e\phi(z)/T_e$. The off-axis profiles $\phi(s(z)) = -\int E_\parallel(s)\mathrm{d}s$, with arclength s in the (r, z) plane, are integrated along the same flux surfaces used in figure 2(*b*). We notice that the $z = 0$ potential well has similar depth both on- and off-axis. The density floor truncates the axial electrostatic potential at $z \approx 100$ to 110 cm, so the full potential drop from the mirror throat to the domain's z boundary is not captured in our simulation. In any case, plasma outflow in the expanders is not well modelled by our electron closure, as the outflow is far from thermal equilibrium (e.g. Wetherton *et al.* 2021). We will restrict our attention to central-cell plasma behaviour that we suppose to be unaffected by the expanders.

Figure 3 shows initial ion velocity distributions, as imported into Hybrid-VPIC from CQL3D-m, at the centre of the mirror cell: $z \in (-5.9, 5.9)$ cm for all simulations. Figure 3(*a–d*) sample ions from the plasma's radial edge: $r \in [5.9, 11.8)$ cm for $R_m = 20$; $r \in [11.8, 23.5)$ cm for $R_m = 41$; $r \in [14.7, 29.4)$ cm for $R_m = 64$. Figure 3(*e*) samples ions from the plasma's core: $r \in [0, 2.9)$ cm for $R_m = 20$; $r \in [0, 5.9)$ cm for $R_m = 41$; $r \in [0, 7.4)$ cm for $R_m = 64$. Figure 3(*f–j*) shows ion distributions, selected from the same axial and radial regions as figure 3(*a–e*), after the simulation has reached $t = 6\tau_{\text{bounce}} \approx 6\,\mu$s. Ions diffuse mostly in $v_\perp$; their distribution is continuous and nearly flat across the velocity-space loss-cone boundary. The reduced distribution $F(v_\perp) = \int f \mathrm{d}v_\parallel$ has relaxed to a monotonically decreasing shape, $\mathrm{d}F/\mathrm{d}v_\perp < 0$, at the plasma edge (figure 3*f*); however, the core plasma maintains $\mathrm{d}F/\mathrm{d}v_\perp > 0$ at low $v_\perp$ (figure 3*j*). Some distribution function moments will be used in later discussion. We define $\boldsymbol{B}$-perpendicular and parallel temperatures

https://doi.org/10.1017/S0022377825000480 Published online by Cambridge University Press

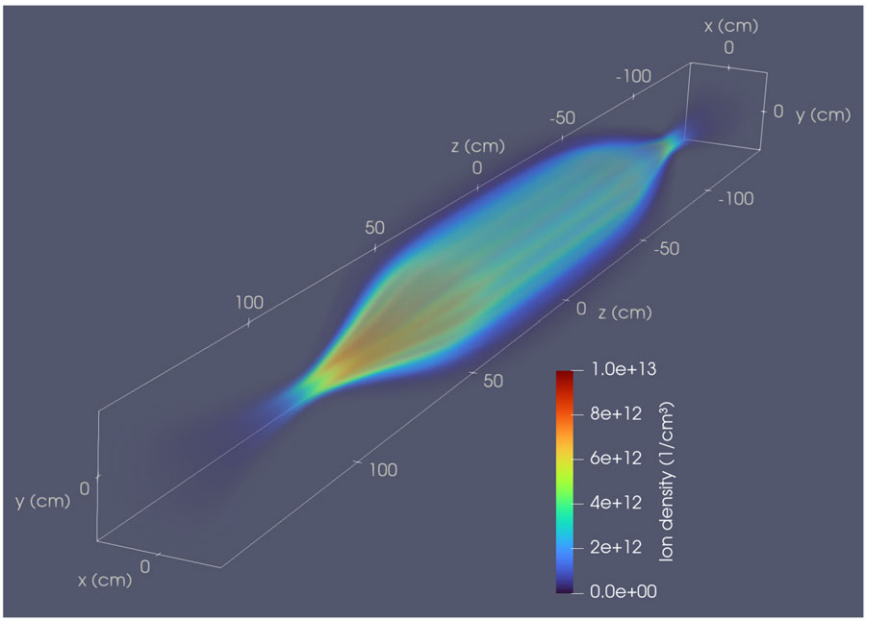

FIGURE 4. The 3-D rendering of ion density in $R_m = 20$ simulation at $t = 6\,\mu$s; colourmap is ion density in units of cm^{-3}. An animated movie is available in the online journal.

$T_{i\perp} \equiv (1/2)\int m_i v_\perp^2 f\,\mathrm{d}\boldsymbol{v}$ and $T_{i\parallel} \equiv \int m_i v_\parallel^2 f\,\mathrm{d}\boldsymbol{v}$ so that $T_i = (2T_{i\perp} + T_{i\parallel})/3$; temperature values for the edge ion distributions at $t = 6\,\tau_{\mathrm{bounce}}$ (figure 3*f–i*) are given in table 1.

Figure 4 shows a 3-D render of ion density in the $R_m = 20$ simulation at $t = 6\,\mu$s. The flute-like ($k_\parallel \sim 0$) nature of the edge fluctuations is apparent. An accompanying movie of the full time evolution from $t = 0$ to $6\,\mu$s is available in the online journal.

To summarize, figures 1–4 show that at the plasma's radial edge: (i) flute-like electrostatic fluctuations appear; (ii) axial outflow and hence losses are enhanced relative to the plasma's core at $r \sim 0$; and (iii) ions diffuse in $v_\perp$ to drive $\mathrm{d}F/\mathrm{d}v_\perp < 0$. It is already natural to suspect that the electrostatic fluctuations diffuse ions into the loss cone and hence cause plasma to escape the mirror.

3.2. *Drift cyclotron mode identification*

To establish the electrostatic mode's nature, we need to know plasma properties at the radial edge and the mode's wavenumber and frequency spectrum.

Figure 5(*a–c,f–h,k–l*) presents the radial structure of the ion density n_i, and the electrostatic fluctuation energy $\delta E_\theta^2 = \langle E_\theta^2\rangle_\theta - \langle E_\theta\rangle_\theta^2$, at the mirror midplane $z = 0$. Figure 5(*d,e,i,j,n,o*) also presents Fourier spectra of density $\tilde{n}_i(m, r)$ and electric component $\tilde{E}_\theta(m, r)$ as a function of azimuthal mode number m and radius r. Beware that Fourier spectrum normalization is arbitrary here and in all figures; Fourier amplitudes may be compared between panels within one figure, but not across distinct figures.

The density gradient $\epsilon \equiv (\mathrm{d}n_i/\mathrm{d}r)/n_i$, in units of inverse ion Larmor radius ρ_{i0}^{-1}, is of order unity and increases with R_m (figure 5*b,g,l*); equivalently, the plasma column

https://doi.org/10.1017/S0022377825000480 Published online by Cambridge University Press

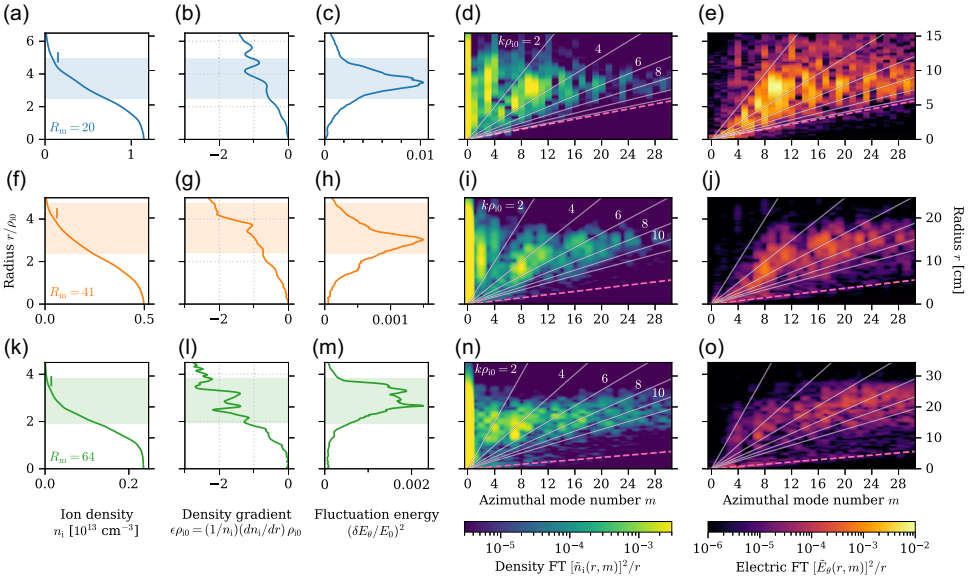

FIGURE 5. Radial structure of plasma at midplane $z = 0$ and at $t = 6\,\tau_{\text{bounce}} \approx 6\,\mu\text{s}$, for simulations with vacuum (*a–e*) $R_m = 20$, (*f–j*) 41, (*k–o*) 64. Panels (*a–c*), (*f–h*) and (*k–l*) show azimuth-averaged radial profiles of (*a*) ion density n_i, (*b*) ion density gradient $\epsilon\rho_{i0}$, (*c*) azimuthal electrostatic fluctuation energy δE_θ^2. Horizontal shaded bars contain the 'edge' ion distributions from figure 3. Vertical dashes in (*a*), (*f*) and (*k*) mark density floor for (2.1). Panels (*d*), (*e*), (*i*), (*j*), and (*n*), (*o*) show azimuthal Fourier spectra of density $\tilde{n}_i(r, m)$ and azimuthal electric field $\tilde{E}_\theta(r, m)$; Fourier transform maps $\theta \to m$, but radius r is not transformed. White rays mark azimuthal wavenumber $k\rho_{i0} = 2, 4, 6, 8, 10, 12$, with $k = m/r$. Dashed pink ray is the maximum $k = \pi/\Delta r$ resolved by the spatial grid, taking $\Delta r = \sqrt{2}\Delta x$. Panels (*f*)–(*j*) and (*k*)–(*o*) are organized similarly.

radius is smaller in units of ρ_{i0} for larger R_m, despite the column's larger physical extent.

The mode spectra of $\tilde{n}$ and $\tilde{E}_\theta$ suggest a partial decoupling of density and electric fluctuations (figure 5, *d, e, i, j, n, o*). In all simulations, low $m \sim 2$–4 density fluctuations are not accompanied by a strong E_θ signal (figure 5*d, e, i, j, n, o*). The $R_m = 20$ simulation shows a strong mode in both density and E_θ fluctuations at $m \approx 9$–10 and equivalent angular wavenumber $k\rho_{i0} \approx 2$–4 (figure 5*d,e*). We identify this Fourier signal with phase-coherent fluting at the same m visible to the eye in figure 1(*b,c*). In contrast, the $R_m = 41, 64$ simulations show a decoupling of density and E_θ fluctuations. The strongest density fluctuations reside at $r \sim 1$–$2\rho_{i0}$, $m \sim 7$–8 and $k\rho_{i0} \approx 2$–6 (figure 5*i,n*), whereas the electrostatic fluctuations reside at larger $r \sim 2$–$4\rho_{i0}$, $m \sim 15$–30 and $k\rho_{i0} \sim 4$–12 (figure 5*j,o*).

The fluctuations have $k_\parallel \ll k_\perp$ and are thus flute-like, which we checked by plotting $\boldsymbol{E}$ in approximate flux-surface coordinates (not shown). Electric-field fluctuations terminate at the mirror throats and do not extend into the expanders; fluctuations may be artificially truncated by the density floor in (2.1).

Joint time-frequency and azimuthal-mode spectra of density and electric field fluctuations, $\tilde{n}(\omega, m)$ and $\tilde{E}_\theta(\omega, m)$, are presented in figure 6(*a–f*). Fluctuations are sampled at radii $r = \{3.34, 2.98, 2.69\}\rho_{i0}$, respectively, over $t = 3$ to $6\,\tau_{\text{bounce}}$; ω is

https://doi.org/10.1017/S0022377825000480 Published online by Cambridge University Press

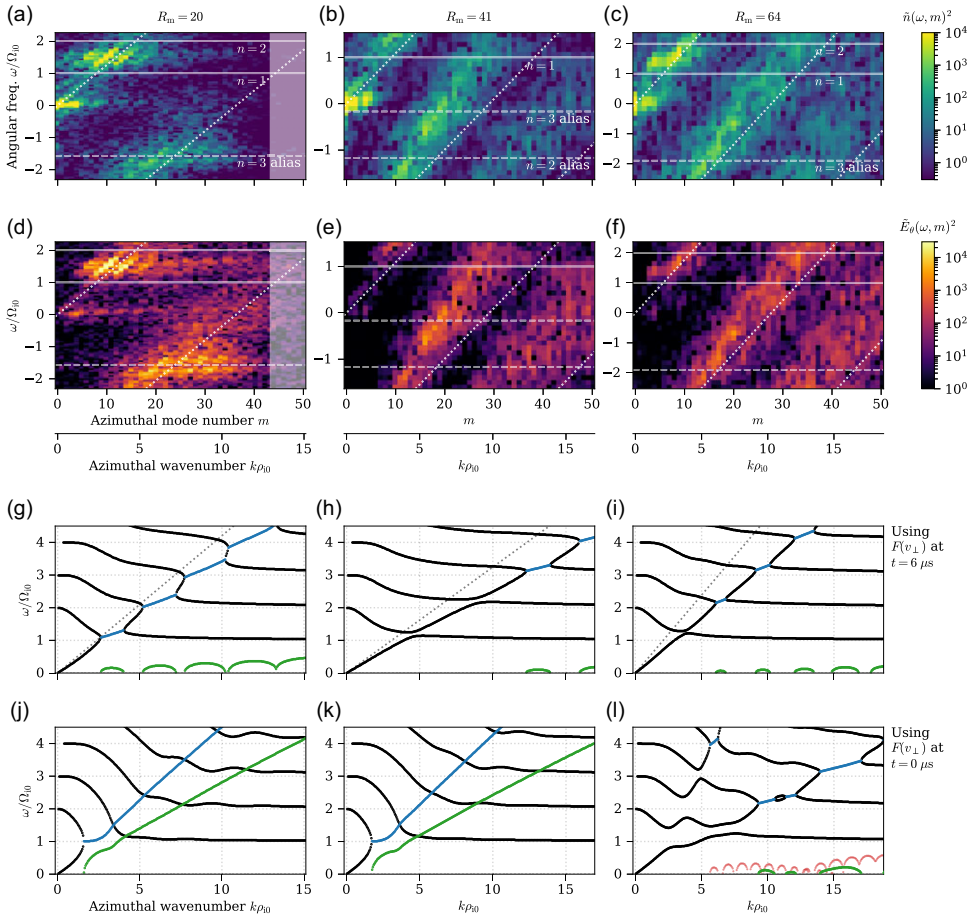

FIGURE 6. Time-azimuth Fourier spectra of density $\tilde{n}(\omega, m)^2$ (*a–c*) and electric field $\tilde{E}_\theta(\omega, m)^2$ (*d–f*) for simulations with $R_m = \{20, 41, 64\}$ (left to right). Panels (*g*)–(*l*) show corresponding (ω, k) of unstable DCLC modes predicted by (3.4) for edge $F(v_\perp)$ at $t \approx 6\,\mu s$ (*g–i*) or $t = 0$ (*j–l*). In panels (*a*)–(*f*), the full ω range within Nyquist-sampling limits is shown; signals with $\omega \gtrsim 2\Omega_{i0}$ alias in frequency. White dotted lines plot ion diamagnetic drift velocity $\omega/k = v_{Di}$. Shaded vertical bar in (*a*), (*d*) marks grid resolution limit $k > \pi/\Delta r$ with $\Delta r = \sqrt{2}\Delta x$. In (*g*)–(*l*), we plot both stable- and unstable-mode frequencies $\mathrm{Re}(\omega)$ (black, blue), and also the corresponding unstable-mode growth rates $\mathrm{Im}(\omega)$ (green). In (*l*) only, red curves plot $\mathrm{Im}(\omega)$ for higher-ω/k modes with $\mathrm{Re}(\omega) \in [4\Omega_{i0}, 14\Omega_{i0}]$ beyond the plot extent. Black dotted lines plot $\omega/k = v_{Di}$.

angular frequency. Positive ω/k corresponds to the ion diamagnetic drift direction. We interpret Fourier power at $\omega < 0$ as high-ω signal that is aliased in frequency space and would otherwise be contiguous in physical (ω, k). Assuming so, both $\tilde{n}$ and $\tilde{E}_\theta$ show a mode spectrum with a phase speed $\omega/k > 0$ comparable to the ion diamagnetic drift speed v_{Di} (white dotted lines, figure 6*a–f*). We compute

$$v_{Di} \approx \frac{T_{i\perp}/m_i}{\Omega_{i0}} \left(-\frac{1}{n_i} \frac{\mathrm{d}n_i}{\mathrm{d}r} \right) = v_{ti0} \frac{T_{i\perp}}{T_{i0}} |\epsilon| \rho_{i0} \tag{3.1}$$

https://doi.org/10.1017/S0022377825000480 Published online by Cambridge University Press

using $\epsilon\rho_{i0} = \{-1, -1, -1.5\}$ and $T_{i\perp}$ measured at $t = 6\tau_{\text{bounce}}$ (values reported in § 3.1). The spectra align with $\omega/k = v_{\text{Di}}$ within a factor of 2.

A fundamental mode appears at $\omega \in [\Omega_{i0}, 2\Omega_{i0}]$ in all simulations. Fluctuation power extends to $\omega \gtrsim 3\Omega_{i0}$ in all simulations, perhaps up to $\omega \gtrsim 7\Omega_{i0}$ in the $R_m = 64$ simulation, but by eye we do not discern discrete harmonics above $2\Omega_{i0}$. A low-frequency $\omega \ll \Omega_{i0}$ mode with non-zero m appears chiefly in $\tilde{n}$ and weakly in $\tilde{E}_\theta$; we identify this slower motion as fluid interchange and discuss it further in § 4.4.

To help interpret figure 6(*a–f*), we compute the linearly unstable (ω, k) for DCLC in a planar-slab plasma with a spatial density gradient ϵ and uniform background magnetic field ($\nabla B = 0$). In such a plasma, a dispersion relation for exactly perpendicular electrostatic waves can be obtained by integrating over unperturbed orbits and Taylor expanding f in particle guiding-centre coordinate, following Stix (1992, § 14–3, (9)). The dispersion relation is then

$$D = 1 + \sum_s \chi_s = 0, \tag{3.2}$$

where the perpendicular ($k = k_\perp$) susceptibility of species s reads

$$\chi_s = \left(\frac{\omega_{ps}}{\Omega_s}\right)^2 \left[\left(1 - \frac{\epsilon\omega}{k}\right) \frac{1}{k^2} \sum_{n=-\infty}^{\infty} \frac{n}{\omega - n} \int \mathrm{d}^3\boldsymbol{v} \left(\frac{1}{v_\perp}\frac{\partial f}{\partial v_\perp}\right) J_n^2 \right.$$
$$\left. - \frac{\epsilon}{k} \sum_{n=-\infty}^{\infty} \frac{1}{\omega - n} \int \mathrm{d}^3\boldsymbol{v}\, f J_n^2 \right]. \tag{3.3}$$

In (3.3), variables are written in a species-specific dimensionless form: $\omega/\Omega_s \to \omega$, $k\rho_s \to k$, $\epsilon\rho_s \to \epsilon$ and $v_\perp/v_{ts} \to v_\perp$, where Ω_s is signed (i.e. $\Omega_e < 0$) and $\rho_s \equiv v_{ts}/\Omega_s$. The decision of how to define v_{ts} (with or without $\sqrt{2}$) is given to the user. The plasma frequency $\omega_{ps} = \sqrt{4\pi n_s q_s^2/m_s}$ for each species. The Bessel functions $J_n = J_n(k_\perp v_\perp)$ as usual, with $k_\perp = k$. Equations (3.2)–(3.3) simplify for cold fluid electrons to yield

$$D = 1 + \chi_i + \frac{\omega_{pe}^2}{\Omega_e^2} + \frac{\omega_{pe}^2}{|\Omega_e|}\frac{\epsilon}{k\omega} = 0, \tag{3.4}$$

where the variables k, ϵ and ω are now in dimensional units. Equation (3.4) is the slab DCLC dispersion relation also used by Lindgren *et al.* (1976, (2)), Ferraro *et al.* (1987, (19)), and Kotelnikov *et al.* (2017, (17) and (A14)). In our sign convention, $\epsilon < 0$ obtains DCLC with $\omega/k > 0$ in the ion diamagnetic drift direction. Equation (3.4) also hosts normal modes with $k < 0$ and high phase velocity in the electron diamagnetic drift direction (Lindgren *et al.* 1976, § 2.A.1.b), which do not appear in our simulations and so are omitted from our discussion.

The unstable- and normal-mode solutions to (3.4), presented in figure 6(*g–l*), are computed as follows. First, we take Ω_{i0}, ρ_{i0} and v_{ti0} as defined in § 2.3 to normalize all variables in (3.4). Plasma parameters used for the $R_m = \{20, 41, 64\}$ simulations, respectively, are $\epsilon\rho_{i0} = \{-1, -1, -1.5\}$; $n_i = \{4, 1.2, 0.5\} \times 10^{12}\ \text{cm}^{-3}$; $B = \{8.6, 4.1, 2.7\} \times 10^3$ G. Both ϵ and n_i describe the plasma edge at the midplane $z = 0$ (figure 5). We take B at $(r, z) = (0, 0)$ to match the variable normalization throughout this manuscript; B at the plasma edge differs by $\lesssim 10\,\%$. Reduced ion distributions $F(v_\perp) = \int f\, \mathrm{d}v_\parallel$ are measured directly from the plasma edge (figure 3). Bessel function sums are computed using all terms with index $|n| \leqslant 40$. The waves

https://doi.org/10.1017/S0022377825000480 Published online by Cambridge University Press

and particles at hand have $k_\perp \rho_{i0} \lesssim 20$ and $v_\perp / v_{ti0} \lesssim 2$, so the Bessel function argument $(k_\perp \rho_{i0})(v_\perp / v_{ti0}) \lesssim 40$. Terms with $n > 40$ contribute little to χ_i because the first positive oscillation of $J_n(\xi)$ peaks at $\xi = j'_n > n$, where j'_n is the smallest positive zero of J'_n (Watson 1922, §15.3), and $J_n(\xi) \to 0$ quickly as $\xi \to 0$ for $\xi \lesssim n$.

We then compute D on a discrete mesh of $(k, \mathrm{Re}(\omega), \mathrm{Im}(\omega))$; for each k, we identify normal modes (whether stable, damped or growing) by seeking local minima of D with respect to the complex ω mesh. Our $D \approx 0$ solutions are not exact. To test our solution scheme, we refined our solutions to $D = 0$ by applying a manual root-finder to each (k, ω) normal mode for one set of plasma parameters, and we saw no significant difference.

Figure 6(*g–i*) uses $F(v_\perp)$ measured from the plasma edge at $t = 6\tau_{\mathrm{bounce}} \approx 6\,\mu\mathrm{s}$, showing DCLC modes at marginal instability (more precisely, drift-cyclotron modes since the loss cone is filled).

Figure 6(*j–l*) uses $F(v_\perp)$ measured at $t = 0$ instead to show that initial distributions with empty loss-cones and spatial gradient $\epsilon \rho_{i0} \sim \mathcal{O}(1)$ drive strongly unstable, broadband electrostatic modes with fastest growth towards high $k\rho_{i0} \gg 1$ and $\omega \gg \Omega_{i0}$. The $R_m = 64$ simulation (figure 6*l*) is an exception, because its CQL3D-m model predicts a larger population of trapped cool ions that helps stabilize DCLC. Figure 6(*l*) also reveals three branches of unstable modes, each with distinct ω/k, that we speculate may be drift waves associated with distinct hot and cool plasma populations (figure 3*a,d*). The slowest branch is visible with $\mathrm{Re}(\omega)$ between 2 to $4\Omega_{i0}$; the corresponding $\mathrm{Im}(\omega)$ are plotted in green. The faster phase speed branches have unstable $\mathrm{Re}(\omega) > 4\Omega_{i0}$ extending to at least $14\Omega_{i0}$; the corresponding $\mathrm{Im}(\omega)$ are plotted in light red.

What is learned from comparing the simulation spectra versus linear theory in figure 6? First, marginally stable DCLC mode growth may explain high $k\rho_{i0} \gtrsim 5$ fluctuations residing in the device during steady-state decay. How do we explain the fundamental mode between $\omega = \Omega_{i0}$ and $2\Omega_{i0}$ for simulations with $R_m = 41, 64$, since that mode is predicted to be linearly stable at late times? It may be an initially excited mode that did not damp and so persists to late times; this appears possible for the $R_m = 41$ simulation, where the fundamental is unstable at $t = 0$. Or, it may be excited by nonlinear flow of wave energy from unstable to stable modes; such an explanation may be needed for the $R_m = 64$ simulation, in which cool plasma at the radial edge should quench DCLC growth of the fundamental mode at both $t = 0$ and $t = 6\,\mu\mathrm{s}$. We have interpreted the $t = 0$ and $t = 6\,\mu\mathrm{s}$ as most- and least-unstable scenarios for DCLC growth, but the plasma may also transition through other states that destabilize the fundamental mode.

3.3. *Ion scattering*

To establish a causal link between δE fluctuations and axial ion losses, we quantify ion scattering in the $R_m = 20$ simulation as follows. We measure velocity jumps over a short time interval $\delta t \equiv t_1 - t_0 = 0.25\Omega_{i0}^{-1}$ for $\mathcal{O}(10^7)$ PIC macroparticles sampled from $|z| \in [0, 5.9]$ cm. Our approach is similar to many other PIC simulation studies; see Yerger *et al.* (2025) for a recent discussion of nuances in constructing and interpreting such velocity jump moments. Figure 7(*a*) shows the probability distribution of the $\boldsymbol{B}$-perpendicular and parallel velocity jumps, $\delta v_\perp = v_\perp(t_1) - v_\perp(t_0)$ and $\delta v_\parallel = v_\parallel(t_1) - v_\parallel(t_0)$. The distributions are not Gaussian and have long tails. The perpendicular jumps $\delta v_\perp$ are much larger than $\delta v_\parallel$, as expected for flute-like ($k_\perp \gg k_\parallel$) electrostatic modes and as evident in figure 3.

https://doi.org/10.1017/S0022377825000480 Published online by Cambridge University Press

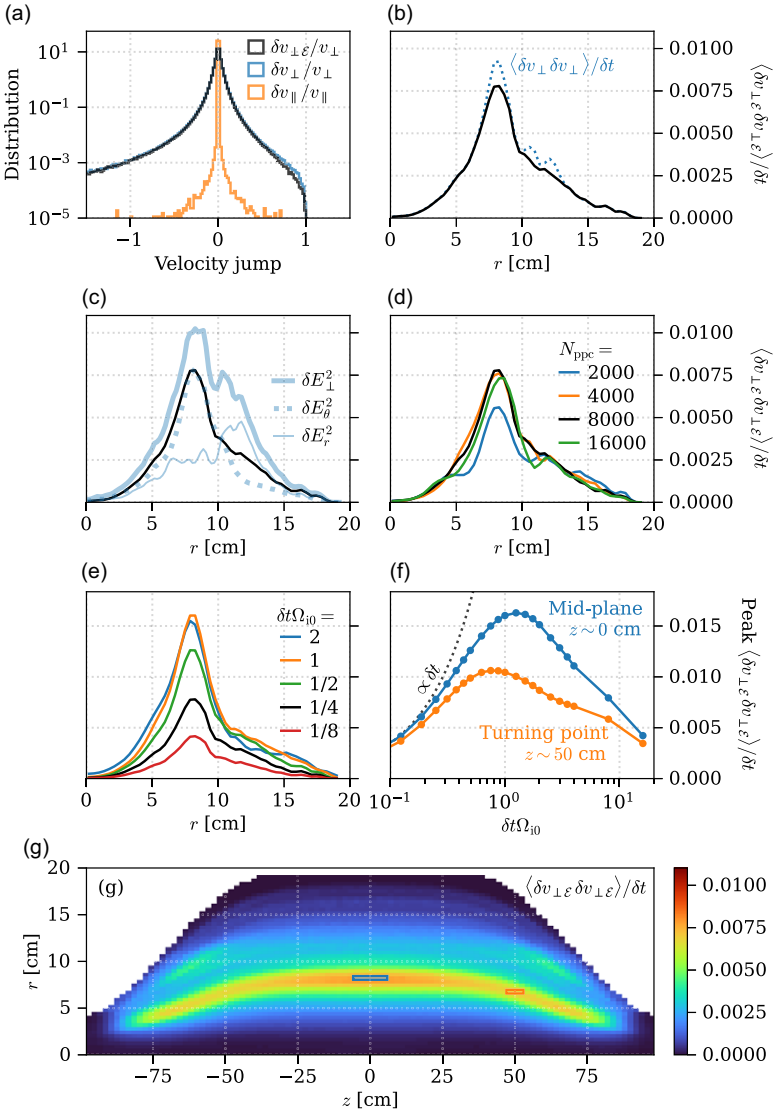

FIGURE 7. Ion scattering measured in $R_m = 20$ simulation, at midplane $z \in [-5.9, 5.9]$ cm unless said otherwise. All diffusion coefficients are normalized to $v_{\rm ti0}^2\Omega_{\rm i0}$. (*a*) Probability distribution of ion velocity jumps, normalized to $v_\perp(t_1)$ and $v_\parallel(t_1)$, for particles at all radii. (*b*) Radial profile of ion diffusion $\langle\delta v_{\perp\mathcal{E}}\delta v_{\perp\mathcal{E}}\rangle/\delta t$ (solid black) compared with $\langle\delta v_\perp\delta v_\perp\rangle/\delta t$ (dotted blue). (*c*) Predicted radial profile of ion diffusion due to fluctuating fields δE_θ^2 (dotted blue), δE_r^2 (thin solid blue), and $\delta E_\perp^2 = \delta E_\theta^2 + \delta E_r^2$ (thick solid blue), compared with $\langle\delta v_{\perp\mathcal{E}}\delta v_{\perp\mathcal{E}}\rangle/\delta t$ (black). (*d*) Numerical convergence in particles per cell for radial profile of $\langle\delta v_{\perp\mathcal{E}}\delta v_{\perp\mathcal{E}}\rangle/\delta t$. (*e*) Effect of measurement time δt upon radial profile of $\langle\delta v_{\perp\mathcal{E}}\delta v_{\perp\mathcal{E}}\rangle/\delta t$. (*f*) Effect of measurement time δt upon diffusion measured at the midplane $(r, z) \approx (8.2, 0)$ cm (blue curve), and near the beam-ion turning point at $(r, z) \approx (6.8, 50)$ cm (orange curve). (*g*) The 2-D map of diffusion $\langle\delta v_{\perp\mathcal{E}}\delta v_{\perp\mathcal{E}}\rangle/\delta t$ computed in discrete (r, z) bins (pixels); only bins with > 100 particles are shown. Light blue and orange boxes mark measurement locations used in (f).

https://doi.org/10.1017/S0022377825000480 Published online by Cambridge University Press

Ion velocities may jump due to both adiabatic and non-adiabatic motion. To separate these motions, introduce an energy $\mathcal{E} = m_i v^2/2 + e\langle\phi\rangle_{\theta,t}$, where $\langle\cdots\rangle_{\theta,t}$ is an average over both azimuth angle θ and time from t_0 to t_1. We expect $\mathcal{E}$ to be conserved by particles gyrating in slowly varying $\boldsymbol{E}$ and $\boldsymbol{B}$ fields, at lowest order in a Larmor-radius expansion. Therefore, we attribute jumps in $\mathcal{E}$ to a non-adiabatic kick in perpendicular velocity that we call $\delta v_{\perp\mathcal{E}}$. We use $\delta\mathcal{E} = \mathcal{E}(t_1) - \mathcal{E}(t_0) = m v_\perp \delta v_{\perp\mathcal{E}} - m(\delta v_{\perp\mathcal{E}})^2/2$ to compute

$$\frac{\delta v_{\perp\mathcal{E}}}{v_\perp(t_1)} = 1 - \sqrt{1 - \frac{2\delta\mathcal{E}}{m v_\perp^2(t_1)}}. \tag{3.5}$$

Equation (3.5) requires $\delta\mathcal{E}$ to not exceed the particle's final perpendicular energy:

$$\delta\mathcal{E} < m v_\perp^2(t_1)/2. \tag{3.6}$$

Figure 7(*a*) shows that the probability distribution of $\delta v_{\perp\mathcal{E}}$, computed only for those particles satisfying (3.6), is marginally narrower than that of $\delta v_\perp$, as expected if non-adiabatic kicks are the main contribution to $\delta v_\perp$.[5]

The ion diffusion $\langle\delta v_{\perp\mathcal{E}}\delta v_{\perp\mathcal{E}}\rangle/\delta t$ as a function of radius is shown in figure 7(*b*); its value is normalized to $v_{\mathrm{ti0}}^2\Omega_{\mathrm{i0}}$ in all of figure 7(*b–g*). Here, $\langle\cdots\rangle$ is a velocity-distribution moment computed in radial bins. The use of $\delta v_{\perp\mathcal{E}}$ decreases the measured diffusion as compared with $\langle\delta v_\perp\delta v_\perp\rangle/\delta t$, as expected.

The ion diffusion due to fluctuating fields $\delta E_\perp(\boldsymbol{r})$ can be described by a diffusion coefficient similar to those used in quasilinear models,

$$D_{\perp\perp} = \frac{1}{2}\left(\frac{e}{m_i}\delta E_\perp\right)^2 \tau_{\mathrm{c}}, \tag{3.7}$$

where τ_{c} is a yet-unknown wave–particle correlation time. Equation (3.7) assumes (i) weak but coherent kicks $\delta v_\perp \approx (e/m_i)\delta E_\perp \tau_{\mathrm{c}}$; (ii) a uniform random distribution of angles between $\boldsymbol{v}_\perp$ and $\delta\boldsymbol{E}_\perp$ to obtain a factor of $1/2$ accounting for kicks in gyrophase instead of $v_\perp$ magnitude. For a scattering-measurement time $\delta t < \tau_{\mathrm{c}}$, we expect

$$D_{\perp\perp} \approx \frac{\langle\delta v_{\perp\mathcal{E}}\,\delta v_{\perp\mathcal{E}}\rangle}{\delta t}, \tag{3.8}$$

also replacing $\tau_{\mathrm{c}} \to \delta t$ in $D_{\perp\perp}$.

Choosing $\delta t < \tau_{\mathrm{c}}$ is unusual for studies of particle diffusion, as the resulting (3.8) describes a more 'ballistic' than diffusive process. But, a short δt helps us. When using a longer $\delta t \gg \tau_{\mathrm{c}}$, at least two issues arise. First, ions gyrate in and out of the scattering zone, as the zone's radial width is similar to an ion Larmor radius. A typical ion may get one or a few kicks, gyrate out of the scattering zone and drift adiabatically, re-enter the scattering zone to be kicked again, and so on, resulting in a random walk with intermittent large time gaps. The scattering zone's finite radial width may also introduce bias in the correlation time τ_{c}, because a typical inboard (small r) ion gyrating in and out of the scattering zone sees a redshift

[5]We checked that (3.6) does not cause noticeable selection bias for short $\delta t \lesssim \Omega_{\mathrm{i0}}^{-1}$; radial profiles of $\langle\delta v_\perp\rangle$ and $\langle\delta v_\perp\delta v_\perp\rangle$, computed with and without particles excluded by (3.6), appear identical to the eye. For larger δt, particles accumulate order-unity kicks in $v_\perp$ and selection bias appears.

https://doi.org/10.1017/S0022377825000480 Published online by Cambridge University Press

$\omega - k_\perp v_\perp$, whereas a typical outboard (large r) ion instead sees a blueshift $\omega + k_\perp v_\perp$. Second, a longer δt needed to sample multiple gyration periods $2\pi\,\Omega_{i0}^{-1}$ will introduce axial bounce effects. In the $R_m = 20$ simulation, $\tau_{\text{bounce}} \approx 40\Omega_{i0}^{-1}$, and even fewer ion gyrations are executed within τ_{bounce} for the higher R_m cases.

In figure 7(*c*) we compare (3.8) with the ion diffusion measured from individual particles. The fluctuating energy density is azimuth averaged as $\delta E_r^2 = \langle E_r^2\rangle_\theta - \langle E_r\rangle_\theta{}^2$, and similarly for δE_θ^2; the sum $\delta E_\perp^2 = \delta E_\theta^2 + \delta E_r^2$. The diffusion due to δE_θ^2 agrees especially well with the particle measurement, whereas the diffusion due to δE_r^2 agrees less well.

Numerical noise might drive axial losses from the plasma edge in the same way that we are attributing to DCLC, because PIC particle count decreases at the plasma edge. To check this possibility, figure 7(*d*) shows that the measured ion scattering is converged in the number of particles per cell used. We are confident that ion scattering is not due to numerical noise because (i) the DCLC electric fields have much larger energy density than numerical noise at the grid scale, and figure 7(*c*) shows good agreement in radial profiles of electric fields and scattering, (ii) we see weak to no N_{ppc} dependence of scattering rates, whereas if scattering were due to noise, we might expect either an outwards shift in r as N_{ppc} increases (for fixed DCLC amplitude), or a decrease in scattering rate if noise suppresses DCLC amplitude; (iii) ion scattering is clearly anisotropic (figure 7*a*), whereas numerical scattering should be insensitive to $v_\parallel$ versus $v_\perp$ because the grid scale is much smaller than the ion Larmor radius.

In figure 7(*e*) we show the effect of δt upon the radial profiles of measured ion diffusion. Figure 7(*f*) then samples the ion scattering at its radial peak $r = 8.2$ cm (blue curve) and shows its dependence upon many more values of δt. We see that the diffusion moment scales linearly with small δt as expected from (3.8); for comparison, the black dotted line shows an exactly linear correlation with δt. As δt becomes $\gtrsim \Omega_{i0}^{-1}$, waves and particles decorrelate and the diffusion rate begins to fall. We perform a similar calculation at $(r, z) \approx (6.8, 50)$ cm (figure 7*f*, orange curve) to conclude that τ_c is shorter near the fast ion turning point. If $\tau_c \sim 1/\Omega_i$ (where Ω_i varies with z, unlike Ω_{i0}), the lower τ_c can be easily explained by the $2\times$ increase in B magnitude.

Finally, figure 7(*g*) shows $\langle \delta v_{\perp\mathcal{E}} \delta v_{\perp\mathcal{E}}\rangle/\delta t$ as a function of (r, z) in the mirror's central cell. The ion scattering at all z is well localized to the same flux surfaces between beam-ion turning points. Scattering is strongest towards $z = 0$, where the central-cell field is relatively uniform.

We conclude from figure 7(*e,f*) that particle scattering has a longer correlation time τ_c and reaches a larger amplitude at the mirror midplane $z = 0$, as compared with near the beam-ion turning points. Ions at $z = 0$, and throughout the central cell where $B \approx B(z = 0)$, should be more important for regulating DCLC growth and saturation than ions at the turning points.

3.4. *Particle confinement time*

Because the loss cone is full – i.e. $F(v_\perp)$ is roughly constant within the loss cone (figure 3) – our simulated mirrors are a collisionless analogue of the GDT at the Budker Institute (Ivanov & Prikhodko 2017). Ions scatter across the loss-cone boundary as fast as (or faster than) untrapped ions can stream out of the mirror, implying an effective mean free path shorter than the device's length. The particle confinement time $\tau_p \equiv N/|\mathrm{d}N/\mathrm{d}t|$, where N is the total number of ions, then scales

https://doi.org/10.1017/S0022377825000480 Published online by Cambridge University Press

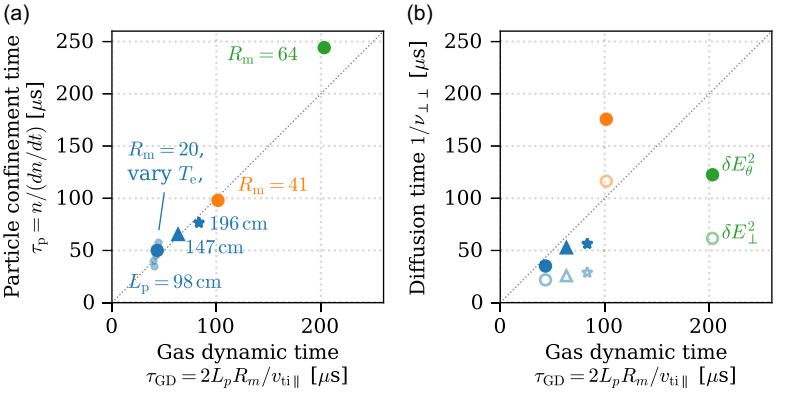

FIGURE 8. (*a*) Particle confinement time measured between $t = 5$ to $6\tau_{\text{bounce}}$, for mirrors of varying R_m (blue, orange, green) and device length L_p (circle, triangle, star markers) as a function of τ_{GD} (3.9). Small blue markers vary T_e for $R_m = 20$; large blue marker is fiducial $T_e = 1.25$ keV. (*b*) Diffusion time scale $1/\nu_{\perp\perp}$ (3.10) modelled from δE_θ^2 (solid markers) and $\delta E_\perp^2$ (hollow markers), as a function of τ_{GD}. In both panels, diagonal dotted line is $\tau_\text{p} = \tau_{\text{GD}}$.

like the eponymous 'gas dynamic' time,

$$\tau_{\text{GD}} = \frac{2L_\text{p}R_m}{v_{\text{ti}\parallel}}, \tag{3.9}$$

adapted from Endrizzi *et al.* (2023, § 3) with $v_{\text{ti}\parallel}$ a characteristic parallel thermal velocity.

To test the relation $\tau_\text{p} \propto \tau_{\text{GD}}$, we measure τ_p between $t = 5$ to $6\,\tau_{\text{bounce}}$, and $v_{\text{ti}\parallel} = \langle v_\parallel^2 \rangle^{1/2}$ at $t = 6\,\tau_{\text{bounce}}$, in each of the $R_m = \{20, 41, 64\}$ simulations with $L_\text{p} = 98$ cm on axis. We also measure τ_p and $v_{\text{ti}\parallel}$ in additional $R_m = 20$ simulations with varying $T_e = 0$, 2.5, 5, 10 keV and longer central cells (larger L_p); the latter are constructed as follows. Split the 'original' mirror device in half at $z = 0$. Between the mirror halves, insert a cylindrical plasma of length 98 or 168 cm, thereby increasing the entire mirror's half-length L_p by 1.5 or 2×. The cylinder has, at all z, the same velocity distribution and magnetic field $\boldsymbol{B}$ as in the original mirror at $z = 0$. The simulation domain is made larger; mesh voxel dimensions (Δx, Δy, Δz) are the same as in § 2. The cylinder's magnetic field is unphysical because it has $\mathrm{d}B_z/\mathrm{d}r \neq 0$ and $B_r = 0$, implying non-zero current $c\nabla \times \boldsymbol{B}/(4\pi)$, so we exclude this current from the $\boldsymbol{j} \times \boldsymbol{B}$ term in Ohm's law(2.1).

The confinement time $\tau_\text{p} \sim \mathcal{O}(10^2)$ µs, and τ_p scales linearly with τ_{GD} as expected (figure 8*a*). Gas-dynamic confinement explains losses from the $R_m = 20$ and 41 simulations very well. Raising electron temperature T_e from 0 to 10 keV lowers τ_p from 57 to 35 µs for the $R_m = 20$ simulations. For comparison, the collisional (aka 'classical') confinement time is 0.1–0.2 s, using (3.4) of Endrizzi *et al.* (2023) with $n = 3 \times 10^{13}$ cm^{-3}, $R_m = 20$ to 64, and beam energy 25 keV.

The $R_m = 64$ shows 20 % better particle confinement than predicted by (3.9). Why? The larger plasma radius and hence longer flux-tube length $> 2L_\text{p}$ between mirror throats only explains ∼5 % of the disagreement. We speculate that electrostatic potential effects may explain the remaining disagreement. In the $R_m = 20$, 41 cases, beam ions diffuse in $v_\perp$ and escape with high $v_\parallel$; electrostatic effects are weak since $T_e \ll T_i$, so (3.9) accurately describes the beam ion confinement. The $R_m = 64$

https://doi.org/10.1017/S0022377825000480 Published online by Cambridge University Press

case has more cool, low-temperature ions (figure 3*i*) that can be trapped by the sloshing-ions' potential peak at $z \sim 30$ cm (Kesner 1973, 1980); confinement is thus improved.

Instabilities in many settings are self-regulating; i.e. unstable waves drive phase-space flow that quenches the waves' own energy source, driving the system to equilibrium (e.g. Kennel & Petschek 1966). If DCLC self-regulates, then we may expect its amplitude to grow in time until the diffusion rate into the loss cone balances the axial outflow rate: $\nu_{\perp\perp} \propto \tau_{\rm GD}^{-1}$. We test this by computing a diffusion rate into the loss cone as

$$\nu_{\perp\perp} \equiv \frac{1}{N_\ell} \int \frac{D_{\perp\perp}(r)}{{v_{\perp \rm LC}}^2} n_i(r) 2\pi r \ell \, {\rm d}r, \tag{3.10}$$

which is a density-weighted average of $D_{\perp\perp}$ (3.7) over a cylindrical kernel of axial length ℓ and radial profile $n_i(r)$, normalized to $N_\ell = \int n_i(r) 2\pi r \ell {\rm d}r$. We take $v_{\perp \rm LC} = v_{\rm ti\parallel}/\sqrt{R_m - 1}$ to approximate the ions' $v_\perp$ at the loss cone boundary, we take $\ell = 12$ cm centred at $z = 0$, and we take $\tau_{\rm c} = \Omega_{\rm i0}^{-1}$. Given these assumptions, and given that (3.7) is not from a self-consistent quasilinear theory, we interpret (3.10) as no more accurate than an order-of-magnitude scaling. In figure 8(*b*) we compute the diffusion time scale $1/\nu_{\perp\perp}$ using either δE_θ^2 or $\delta E_\perp^2$ as defined as in figure 7(*c*). We observe that $1/\nu_{\perp\perp}$ has similar magnitude as $\tau_{\rm GD}$, as expected. But, no trend is obvious from the scatter and few data points.

4. Discussion

4.1. *Cool plasma effects*

How much cool plasma, and at what temperature, suppresses DCLC for the peaked beam-ion distributions injected into WHAM? To answer this, figure 9 computes DCLC linear stability with distinct 'hot' and 'cool' ion populations. The hot ions are a beam distribution at $t = 0$ in our $R_m = 20$ simulation, taken from the midplane $z = 0$ (figure 3*b*), with $n_{\rm hot} = 4 \times 10^{12}$ cm^{-3}. The cool ions are a Maxwellian of the same species (deuterium), with density $n_{\rm cool}$ and temperature $T_{\rm cool}$. We solve (3.4) using the same procedure as in § 3.2, within a finite domain $k\rho_{\rm i0} < 15$, ${\rm Re}(\omega)/\Omega_{\rm i0} < 10$, and ${\rm Im}(\omega)/\Omega_{\rm i0} < 4$.

Figure 9(*a*) predicts that DCLC is suppressed when cool and hot ion densities are nearly equal, and $T_{\rm cool} \sim 2$ to 10 keV. In cases where DCLC is not fully stabilized, figure 9(*b*) shows that dense-enough cold plasma will at least stabilize low cyclotron harmonics; we anticipate that the remaining unstable high harmonics may have weaker scattering rate. Figure 9(*b*) qualitatively concurs with recent measurements on the GDT device: DCLC at high harmonics appeared when a relatively high gas density was puffed into GDT's central chamber before neutral-beam injection (Prikhodko *et al.* 2018; Shmigelsky *et al.* 2024); critically, this form of DCLC did not impede the build-up of plasma pressure. Figure 9(*c–h*) show the effect of varying $T_{\rm cool}$ (with $n_{\rm cool} = n_{\rm hot}$) upon DCLC mode structure in (ω, k). As $T_{\rm cool}$ rises, quenching of low harmonics proceeds to total stabilization. When $T_{\rm cool}$ is too high and near the beam ions' effective temperature, the 'cool' plasma is less able to reduce the velocity-space gradient ${\rm d}F/{\rm d}v_\perp$ and DCLC becomes unstable at all harmonics.

To test the predictions of figure 9, we repeat the $R_m = 20$ Hybrid-VPIC simulation with cool plasma added to the radial edge, varying $n_{\rm cool} \approx \{4, 8, 16\} \times 10^{12}$ cm^{-3} within radii $r \sim 5$ to 12 cm (figure 10*a*) and also varying $T_{\rm cool} = \{1, 2, 5\}$ keV. The simulation results are summarized in figure 10(*b–i*).

https://doi.org/10.1017/S0022377825000480 Published online by Cambridge University Press

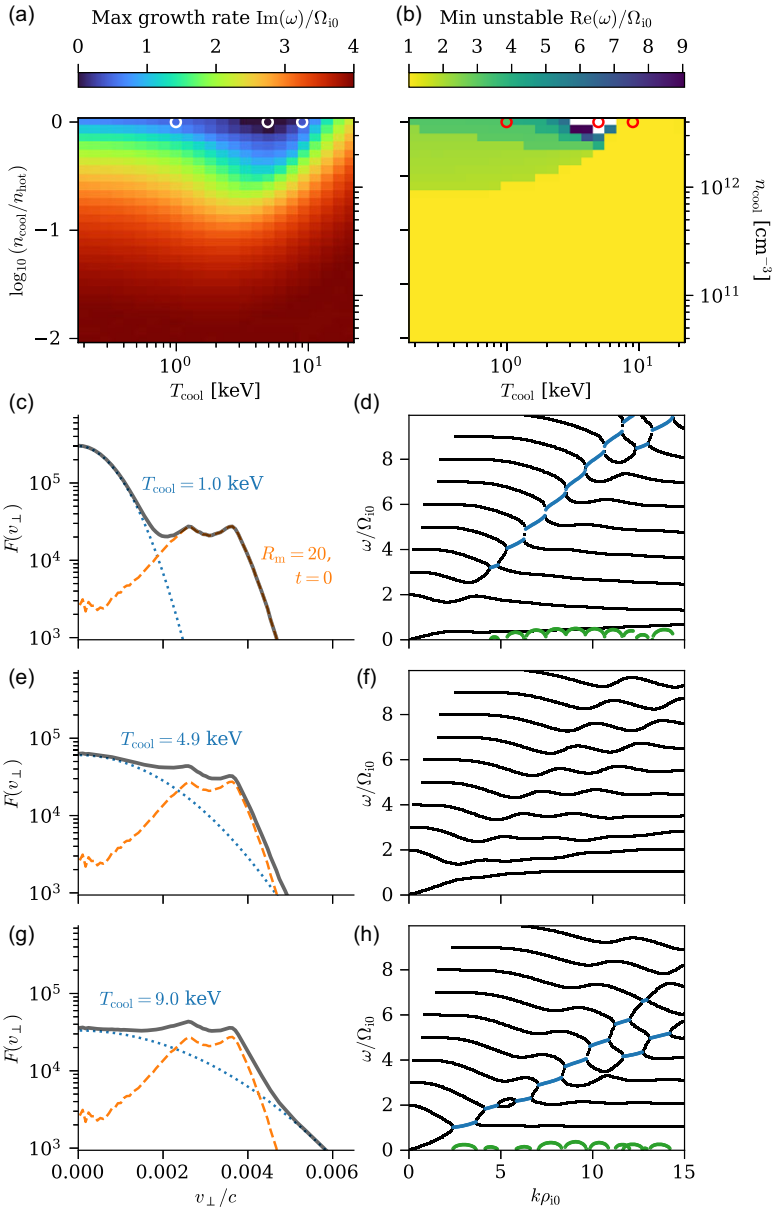

FIGURE 9. Effect of cool plasma on DCLC linear stability in WHAM with $R_m = 20$ and a hot beam-ion distribution. (*a*): The 2-D regime map of maximum growth rate $\mathrm{Im}(\omega)/\Omega_{i0}$ as a function of n_{cool} and T_{cool}. (*b*) Like (*a*), but showing minimum $\mathrm{Re}(\omega)/\Omega_{i0}$ that is DCLC unstable. As cool plasma density is raised, low harmonics are stabilized. White pixels in (*b*), at $T_{\mathrm{cool}} \sim 5$ keV and $\log_{10}(n_{\mathrm{cool}}/n_{\mathrm{hot}}) \sim 0$, mean that no linearly unstable modes were found. (*c*) Example ion distribution $F(v_\perp)$ with 1 keV cool plasma (dotted blue) added to initial $R_m = 20$ distribution. (*d*) Dispersion relation solutions corresponding to (*c*), showing normal modes (black), unstable mode $\mathrm{Re}(\omega)$ (blue) and unstable mode $\mathrm{Im}(\omega)$ (green). (*e, f*) Like (*c, d*), but with 4.9 keV cool plasma. (*g, h*) Like (*c, d*), but with 9.0 keV cool plasma.

https://doi.org/10.1017/S0022377825000480 Published online by Cambridge University Press

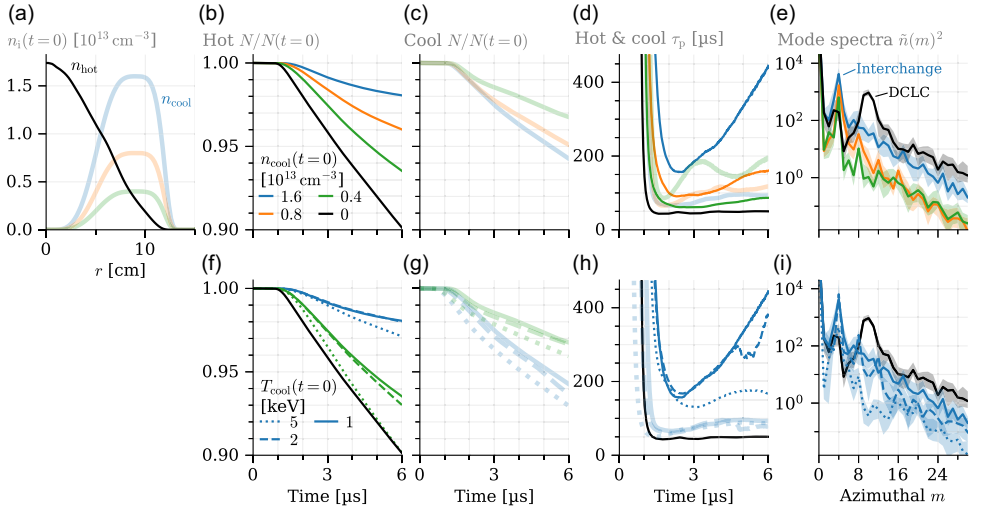

FIGURE 10. Effect of cool plasma on particle losses and density fluctuations in Hybrid-VPIC simulations with $R_m = 20$. (*a*) Initial density radial profiles for hot (black) and cool (coloured) ions. (*b*) Total number of hot ions within simulation domain, normalized to initial value, for varying n_{cool} at fixed $T_{cool} = 1$ keV. (*c*) Like panel (*b*), but for cool ions. (*d*) Particle confinement time $\tau_p = N/(dN/dt)$ for hot and cool populations, same simulations as in (*b*) and (*c*). (*e*) Fourier spectra of azimuthal density fluctuations, using total (hot plus cool) ion population; solid lines are median and shading is 25–75 percentile range within 3–6 μs. (*f*)–(*i*) Like (*b*)–(*e*), but emphasis on varying $T_{cool} = \{1, 2, 5\}$ keV at fixed n_{cool}. Curve styles are matched across all panels.

Cool 1 keV plasma quenches DCLC losses and improves the hot plasma's final $N/N(t=0)$ by a factor of ∼2 to 5× (figure 10*b*). The hot plasma's final confinement time is at most $\tau_p = 445$ μs, a stark improvement over $\tau_p = 50$ μs without cool plasma (figure 10*d*). The cool plasma itself is less well confined with $\tau_p \lesssim 200$ μs (figure 10*d*), but it may be externally replenished in real experiments or in more realistic future simulations. The simulation with lowest $n_{cool} = 4 \times 10^{12}$ cm^{-3} shows that cool ions are better confined than the hot ions, qualitatively consistent with trapping by the sloshing ions' axial potential (figure 10*b,c*). The situation reverses at higher n_{cool}: hot ions become better confined than cool ions, which we speculate may be due to flattening of ion density n, and hence also electric potential ϕ, along z.

Azimuthal fluctuations in density confirm that cool plasma quenches DCLC at $m \approx 10$ (figure 10*e*). But, cool ions also drive faster-growing MHD interchange-like modes at $m \approx 4$. If our simulations were run longer than $t = 6$ μs, these interchanges might eventually cause large ion losses. In laboratory devices, interchange can be stabilized by shear flow driven by either external voltage biasing (Beklemishev *et al.* 2010; Yakovlev *et al.* 2018) or electron cyclotron heating (Yoshikawa *et al.* 2019). We thus remain optimistic that cool plasma stabilization can work in WHAM, especially given the method's success in real laboratory experiments (Coensgen *et al.* 1975; Shmigelsky *et al.* 2024). In §4.4, we will comment further on interchange identification and growth/suppression.

The Hybrid-VPIC simulations quench DCLC losses at higher n_{cool}/n_{hot} and lower T_{cool} than predicted by the linear theory. The hot-ion confinement is worse with

https://doi.org/10.1017/S0022377825000480 Published online by Cambridge University Press

$T_{\rm cool} = 5\,{\rm keV}$ as compared with lower $T_{\rm cool}$ (figure 10*f–h*), which contrasts with the prediction of figure 9 that $T_{\rm cool} = 5\,{\rm keV}$ with $n_{\rm cool} \approx n_{\rm hot}$ fully stabilizes DCLC within a wide (k, Re(ω), Im(ω)) domain. Why does $T_{\rm cool} \sim 1\,{\rm keV}$ work better than 5 keV? It may be explained by some combination of (i) weaker electrostatic trapping and faster outflow $v_{{\rm ti}\parallel}$ as $T_{\rm cool}$ increases, and (ii) quasilinear diffusion of beam ions towards the loss cone, which shifts the unstable drive $\mathrm{d}F/\mathrm{d}v_\perp$ to lower $v_\perp$ so that lower $T_{\rm cool}$ becomes stabilizing.

Let us expand on point (ii). For a quasilinearly diffused $F(v_\perp)$, the relevant $T_{\rm cool}$ is set not by the injected beam distribution, but instead by the loss-cone's $v_\perp$ boundary value at the injected beam's characteristic $v_\parallel$. For WHAM's 45° pitch-angle beam, DCLC-scattered ions escape at the loss-cone boundary with perpendicular energy,

$$m_i v_\perp^2/2 \sim E_{\rm beam} \cos^2\theta_{NBI}/(R_m - 1) \approx 0.7\,{\rm keV}, \tag{4.1}$$

using $E_{\rm beam} = 25\,{\rm keV}$, $\theta_{NBI} = 45°$, and $R_m = 20$. Equation (4.1) agrees with the $T_{\rm cool} = 1\,{\rm keV}$ stabilization in our simulations (figure 10).

It is interesting to contrast WHAM with 2XIIB, which used 90° pitch-angle beam injection. In 2XIIB, DCLC-scattered ions have $v_\parallel \sim 0$ and therefore escape at the loss-cone boundary with perpendicular energy

$$m_i v_\perp^2/2 \sim q_i \Delta\phi/(R_m - 1) \sim 0.2 - 0.5\,{\rm keV} \tag{4.2}$$

using $q_i\Delta\phi \sim (2-5) \times T_e$, $T_e \approx 100\,{\rm eV}$ and $R_m = 2$ (Coensgen *et al.* 1975); here $\Delta\phi$ is the axial potential drop from midplane to throat (Baldwin 1977, § V.B). So, we may bear in mind that the appropriate $T_{\rm cool}$ to stabilize DCLC (and the parametric dependence of $T_{\rm cool}$ upon either $E_{\rm beam}$ or $\Delta\phi$) is mediated by the beam injection angle in a given device.

4.2. *Spatial gradient effects*

A smaller spatial gradient $\epsilon\rho_{\rm i0}$ also helps to stabilize DCLC (Baldwin 1977; Correll *et al.* 1980; Ferron & Wong 1984). Figure 11 shows this for plasma parameters similar to the physically larger, break-even axisymmetric mirror (BEAM) design concept of Forest *et al.* (2024). We recompute DCLC linear stability for BEAM's radial edge comprising (i) hot deuterium and tritium beam ions, with equal densities of deuterium and tritium, and temperature $T \approx 60\,{\rm keV}$ (Forest *et al.* 2024, figure 6), and (ii) cool Maxwellian ions with varying $n_{\rm cool}$, $T_{\rm cool}$ and isotope choice of hydrogen, deuterium, tritium or a deuterium–tritium mixture (equal densities of deuterium and tritium). The stability calculation assumes $\epsilon\rho_{\rm i0} = -0.04$, $B = 3\,{\rm T}$ and $n_{\rm hot} = 6 \times 10^{13}\,{\rm cm}^{-3}$ counting both deuterium and tritium species. The value $1/|\epsilon\rho_{\rm i0}| = 25$ approximately matches the DCLC design constraint $a/\rho_i = 25$ used by both Forest *et al.* (2024) and Frank *et al.* 2025. For normalization, we take $\rho_{\rm i0} = 1.2\,{\rm cm}$ and $f_{\rm ci0} = 22.9\,{\rm MHz}$. We solve (3.4) using the same procedure as in § 3.2, within a finite domain $k\rho_{\rm i0} < 30$, ${\rm Re}(\omega)/\Omega_{\rm i0} < 10$ and ${\rm Im}(\omega)/\Omega_{\rm i0} < 5$. The domain is larger than before because DCLC appears at larger $k\rho_{\rm i0}$; the relevant k may be estimated for the nth cyclotron harmonic as $k\rho_{\rm i0} \approx n/(|\epsilon|\rho_{\rm i0})/(T_{\rm i\perp}/T_{\rm i0})$, from requiring that the ion diamagnetic drift $\omega/k = v_{\rm Di}$ intersects the harmonics $\omega = n\Omega_{\rm i0}$. The Bessel sums retain all terms with index $|n| \leqslant 120$ to ensure convergence.

https://doi.org/10.1017/S0022377825000480 Published online by Cambridge University Press

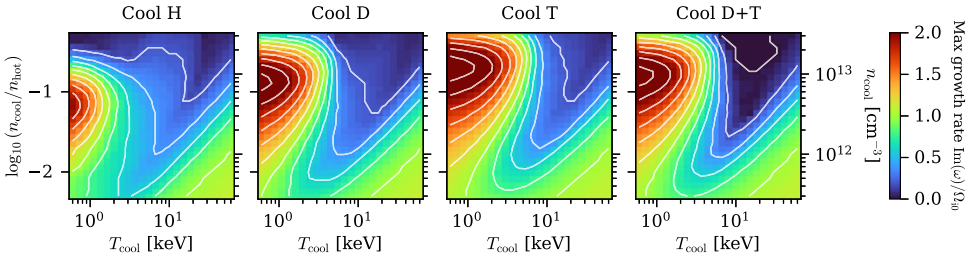

FIGURE 11. Effect of cool plasma on DCLC linear stability in a physically larger next-step mirror, similar to the BEAM concept described in Forest *et al.* (2024), with spatial gradient $|\epsilon|\rho_{i0} = 0.04$ smaller than in WHAM. Each panel shows varying cool plasma composition. For the cool D $*$ T case, $n_{\rm cool}$ counts both D/T species, and the cool D and cool T have equal densities. Total stabilization $\mathrm{Im}(\omega) \to 0$ is achieved when the cool ions' isotopes are matched to that of the hot ions. Colourmap range in $\mathrm{Im}(\omega)$ is reduced from figure 9(*a*).

Figure 11 predicts that a larger region of the parameter space ($n_{\rm cool}/n_{\rm hot}$, $T_{\rm cool}/T_{\rm hot}$) becomes available to help stabilize DCLC in a BEAM-like concept. Complete stabilization $\mathrm{Im}(\omega) \to 0$ occurs when the cool plasma is a deuterium–tritium mixture like the hot plasma, following the empirical 'spectral rule' of Kotelnikov & Chernoshtanov (2018). For cool plasma of pure hydrogen, deuterium or tritium, we find that $\mathrm{Im}(\omega)$ is reduced but generally remains non-zero; the remaining unstable modes have ω at the hot-ion cyclotron harmonics not overlapped by the cool-ion harmonics, as previously shown by Kotelnikov & Chernoshtanov (2018).

Both Tang *et al.* (1972, figure 1) and Baldwin (1977, figure 7) also computed the maximum radial gradient ϵ for DCLC to be stable, as a function of the density-proxy parameter $(\Omega_i/\omega_{\rm pi})^2$. For WHAM, $\epsilon\rho_{i0} \sim 1$ is DCLC unstable for nearly all values of $(\Omega_i/\omega_{\rm pi})^2$ anyway. For the model BEAM plasma in figure 11, we find $(\Omega_i/\omega_{\rm pi})^2 \sim 3 \times 10^{-4}$ requires low $\epsilon\rho_{i0} \sim 0.01$ for stability, so it is reasonable that our model with $|\epsilon\rho_{i0}| \sim 0.04$ remains DCLC unstable in the absence of cool plasma.

Though figure 11 suggests that a BEAM-like concept may be DCLC unstable, we note that many mitigating factors remain. First, BEAM-sized plasmas need much lower $n_{\rm cool}$ to stabilize DCLC as compared with WHAM, as expected from previous work (Baldwin 1977); there are many ways to craft such cool plasma in the laboratory. Second, the peaked beam-ion distributions used here may be viewed as 'maximally' unstable; quasilinear diffusion will smooth ion distributions towards marginal stability, as discussed in §§ 3.4 and 4.1. Third, our calculation neglects physical effects such as finite plasma β (i.e. ∇B along r) and both radial and axial geometry; these effects are generally thought to aid stability (Tang *et al.* 1972). Fourth, recall from figure 9 that even if DCLC remains unstable, it can be rendered less harmful by pushing $\mathrm{Re}(\omega)$ to high harmonics of Ω_{i0} and so reducing DCLC's scattering rate, as shown on the GDT device (Shmigelsky *et al.* 2024). Fifth, the plasma parameters in figure 11 are only an example; no attempt was made, for this manuscript, to optimize parameters beyond what was discussed in Forest *et al.* (2024). Lastly, we recall that DCLC has been successfully mitigated in past and current mirror devices, including two that used WHAM/BEAM-like sloshing-ion injection: TMX-U and GDT.

As an aside, the 2-D parameter-regime maps of figures 9(*a*) and 11 show interesting structure that has been studied in detail by Gerver (1976, figures 1, 3

https://doi.org/10.1017/S0022377825000480 Published online by Cambridge University Press

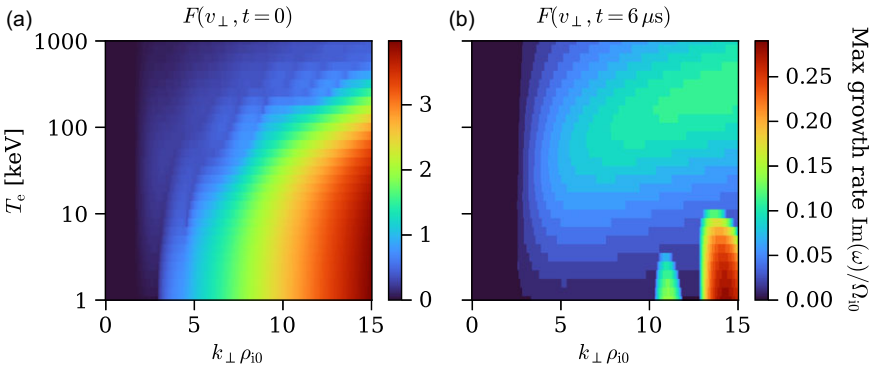

FIGURE 12. Effect of parallel-kinetic electron response upon DCLC linear stability, using ion distributions from the WHAM $R_m = 20$ simulation at either $t = 0$ to obtain a beam-ion distribution (a), or at $t = 6\,\mu$s to obtain a saturated distribution with $\mathrm{d}F/\mathrm{d}v_\perp < 0$ (b).

and 4); Gerver used a subtracted-Maxwellian distribution for hot ions, unlike our arbitrary beam-ion distributions, but his results agree qualitatively with ours. For example, figure 11 shows that at low $T_{\mathrm{cool}}/T_{\mathrm{hot}}$, a distinct instability occurs even at large $n_{\mathrm{cool}}/n_{\mathrm{hot}} \gtrsim 10^{-1}$; it is called double-humped instability by Baldwin (1977) and Kotelnikov *et al.* (2017) or ion two-temperature instability by Gerver (1976). The interested reader may consult Gerver (1976), Baldwin (1977), Post (1987)and Kotelnikov *et al.* (2017) for more thorough treatments and reviews of DCLC linear-stability physics.

4.3. *Kinetic electron effects*

Our linear dispersion relation assumed $k = k_\perp$, neglecting both ion and electron parallel responses. But, $k_\parallel \sim \pi/(2L_{\mathrm{p}})$ is imposed by the mirror geometry for the lowest possible axial harmonic. In WHAM with $R_m = 20$, electrons with $T_e \sim 1$ keV have thermal velocity v_{te} similar to DCLC parallel phase velocity $\omega/k_\parallel \sim \Omega_{i0}/k_\parallel$, so DCLC modes may be Landau damped by electrons.

We qualitatively assess the effect of parallel electron kinetics in (3.4) by replacing the perpendicular, cold-fluid electron susceptibility,

$$\chi_e = \frac{\omega_{\mathrm{pe}}^2}{\Omega_e^2} + \frac{\omega_{\mathrm{pe}}^2}{|\Omega_e|}\frac{\epsilon}{k\omega}, \tag{4.3}$$

with a more general form for oblique electrostatic waves that includes a $\boldsymbol{B}$-parallel kinetic response,

$$\chi_e = -\left(\frac{k_\perp}{k}\right)^2 \frac{\omega_{\mathrm{pe}}^2}{\Omega_e^2}\left[1 + \frac{\epsilon|\Omega_e|}{k_\perp \omega}\right]\zeta_{0\mathrm{e}} Z(\zeta_{0\mathrm{e}}) - \left(\frac{k_\parallel}{k}\right)^2 \frac{\omega_{\mathrm{pe}}^2}{k_\parallel^2 v_{\mathrm{te}}^2} Z'(\zeta_{0\mathrm{e}}). \tag{4.4}$$

Here Z is the plasma dispersion function, $\zeta_{0\mathrm{e}} = \omega/(k_\parallel v_{\mathrm{te}})$, and $v_{\mathrm{te}} = \sqrt{2T_e/m_e}$. We fix $k_\parallel = \pi/(2L_{\mathrm{p}})$ to mimic a fundamental-harmonic mode along the device axis. Both (4.3) and (4.4) are dimensional. The derivation is briefly sketched in Appendix B.

Figure 12 recomputes DCLC linear stability, using (4.4) to show the effect of parallel electron kinetics, for the ion distributions from our WHAM $R_m = 20$ simulation at $t = 0$ and $t = 6\,\tau_{\mathrm{bounce}} \approx 6\,\mu$s. Figure 12($a$) shows that the $t = 0$, peaked beam-ion

https://doi.org/10.1017/S0022377825000480 Published online by Cambridge University Press

distribution with empty loss cone remains unstable for a broad range of k; electron kinetics do not stabilize a strongly peaked and hence strongly unstable $F(v_\perp)$. In contrast, figure 12(*b*) shows that the marginally unstable $t = 6\,\mu$s distribution with filled loss cone has DCLC growth rates reduced by electron kinetics.

In the limit $T_e \to \infty$, $\zeta_{0e} \to 0$ suppresses the electron parallel susceptibility; i.e. the $(k_\parallel/k)^2$ term in (4.4) asymptotes to $1/(k^2\lambda_{\mathrm{De}}^2)$, where λ_{De} is the electron Debye length, and its magnitude and contribution to D is negligible. More importantly, hot electrons and finite $k_\parallel$ suppress the *perpendicular* drift term in (4.4) by driving $\zeta_{0e}Z(\zeta_{0e}) \to 0$; this disables the coupling between ion Bernstein waves and the drift wave. In figure 12(*b*), at $T_e \gtrsim 50\,$keV the resulting mode structure appears similar to the 'pure' ion Bernstein waves in a homogeneous plasma, but with non-zero growth rates. These unstable Bernstein modes are negative-energy waves satisfying the criterion $\partial\,[\omega\mathrm{Re}(D)]\,/\partial\omega|_{\mathrm{Re}(\omega)} < 0$ (Stix 1992, § 4–2); in this criterion we replaced the Hermitian part of the dielectric tensor with $\mathrm{Re}(D) = \mathrm{Re}(1 + \chi_i + \chi_e)$, which is valid because D has no contributions from off-diagonal terms $\chi_{\parallel\perp}$ in either species' susceptibility tensor. See also Kadomtsev *et al.* (1964), Bers & Gruber (1965) and Baldwin (1977).

In the limit of low $T_e \lesssim 1\,$keV, the perpendicular drift term in (4.4) reverts to its fluid form because $\zeta_{0e}Z(\zeta_{0e}) \to -1$. The parallel term, which asymptotes to $-(k_\parallel/k)^2(\omega_{\mathrm{pe}}/\omega)^2$, is the main new influence on DCLC mode structure. Figure 12(*a*) shows that the $t = 0$ beam-ion distribution is not much affected at low T_e when compared with figure 6(*j*). But, figure 12(*b*) shows that the $t = 6\,\mu$s distribution has low harmonics of DCLC suppressed, and the growth rates of higher harmonics somewhat reduced, by electron kinetics when compared with figure 6(*g*).

Equation (4.4) is less accurate than bounce averaging of unperturbed particle orbits within a specified axial mirror geometry, as has been performed and studied by, for example Cohen *et al.* (1983), Koepke *et al.* (1986*a*) and others. A significant unknown is the effect of the non-monotonic axial electric potential ϕ; since $\phi \sim T_e$ and ϕ can trap electrons at sloshing-ion turning points, electron orbits may be significantly modified. None of this is captured in our Hybrid-VPIC simulations given the simple electron closure. Our goal is only to show qualitatively how parallel electron kinetics, including electron Landau damping, may impact DCLC. We conclude that saturated DCLC amplitude and frequency in WHAM may be tuneable via T_e or other device parameters, as was done on the MIX-1 device previously (Koepke *et al.* 1986*a*; Koepke 1992).

4.4. *Other modes*

Our simulations mostly grow DCLC, but other kinetic and fluid modes can appear in mirror devices (Post 1987). The modes relevant to WHAM were surveyed by Endrizzi *et al.* (2023); here we add a few remarks.

Interchange modes should be stabilized by the effect of finite ion Larmor radius, specifically collisionless gyroviscosity (Roberts & Taylor 1962), when

$$k_\perp \rho_{\mathrm{i}0} > 4\sqrt{\frac{a}{L_{\mathrm{p}}}} \approx 1.3, \tag{4.5}$$

with $a \approx 10\,$cm the plasma column radius and assuming a curvature-driven growth rate $v_{\mathrm{ti}0}/\sqrt{aL_{\mathrm{p}}}$ (Ryutov *et al.* 2011, § III.B). In figure 13, we present new simulations of Maxwellian ions with varying temperature $T_{\mathrm{i}0} = 5$ to $20\,$keV in the WHAM $R_m = 20$ geometry. As $T_{\mathrm{i}0}$ decreases, DCLC weakens in amplitude and spectral width, and

https://doi.org/10.1017/S0022377825000480 Published online by Cambridge University Press

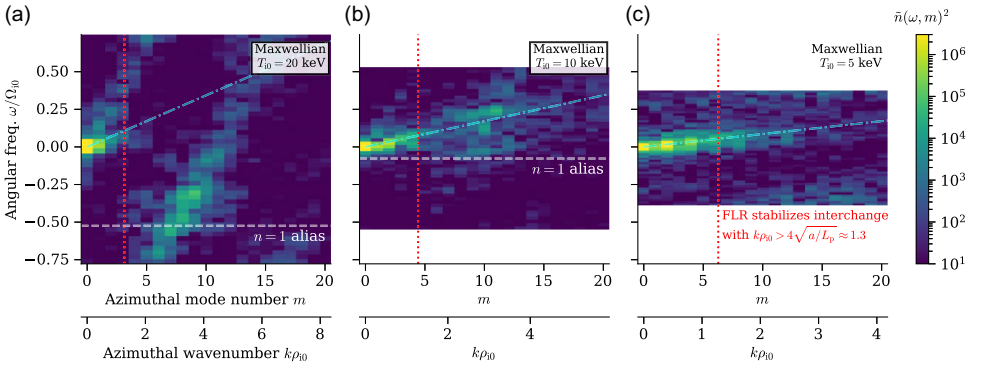

FIGURE 13. Interchange modes appear and DCLC weakens as T_i decreases (*a* to *c*) in simulations of Maxwellian ions in WHAM's $R_m = 20$ magnetic-field geometry. Fourier spectra computed as in figure 6. The dot–dashed cyan line plots the interchange mode's expected phase velocity, $\omega/k = v_{Di}/2$, assuming spatial gradient $\epsilon = (10\,\mathrm{cm})^{-1}$.

a lower-m mode grows in amplitude and spectral width. We identify the lower-m mode as interchange because (i) its phase velocity is half the ion diamagnetic drift and in the same direction (neglecting gravitational drift, which is $\sim(a/L_p)\times$ smaller), consistent with the planar-slab derivation (Rosenbluth *et al.* 1962; Roberts & Taylor 1962); (ii) its k bandwidth qualitatively scales with T_i following (4.5). Note that in this paragraph and figure 13, we redefine $v_{ti0} = \sqrt{2T_{i0}/m_i}$ with a factor of $\sqrt{2}$, which also affects $\rho_{i0} = v_{ti0}/\Omega_{i0}$. We caution that our simulated interchange has relatively strong $m = 2$ and $m = 4$ modes compared with, for example, the odd $m = 3$ mode; this effect may be unphysical, and we suspect mesh imprinting.

Alfvén ion cyclotron (AIC) modes do not appear at significant amplitude in our simulations; recall that both δB_r and δB_θ are small (§ 3.1), and pitch-angle scattering is weak compared with DCLC's $v_\perp$ scattering (figure 3). Does our non-observation agree with theory and prior experiments? An empirical criterion for AIC growth, obtained from experiments on the tandem mirror GAMMA-10 (Ichimura *et al.* 1993; Katsumata *et al.* 1996), is

$$T_{i\perp}/T_{i\parallel} > 0.55/\beta_\perp^{0.5}, \tag{4.6}$$

based on data with $\beta_\perp < 0.03$. One linear-instability criterion, derived for a homogeneous bi-Maxwellian plasma (Gary *et al.* 1994) and with a form commonly used in the solar-wind literature (e.g. Hellinger *et al.* 2006), is

$$T_{i\perp}/T_{i\parallel} > 1 + 0.43/\beta_\parallel^{0.42}. \tag{4.7}$$

At $t = 0$ in our $R_m = 20$ simulation, the sloshing-ion turning points have $\beta_\perp = 8\pi n T_{i\perp}/B^2 = 0.17$ and $\beta_\parallel = 8\pi n T_{i\parallel}/B^2 = 0.068$, with corresponding anisotropy $T_{i\perp}/T_{i\parallel} = 2.5$; our simulations with larger R_m have similar anisotropy and lower plasma beta at the turning points. Both (4.6) and (4.7) indicate that AIC may be unstable at the turning points.

So, why does AIC not appear? First, since AIC is driven by gradients of f on resonant surfaces in velocity space, (4.6) and (4.7) will not be so precise when applied to different ion distributions; for example, Isenberg *et al.* (2013) noted that subtle modifications to f at marginal AIC stability can modify anisotropy thresholds based on bi-Maxwellian temperatures by a factor of $\sim$2. Second, AIC is stabilized by

https://doi.org/10.1017/S0022377825000480 Published online by Cambridge University Press

the inhomogeneous plasma in WHAM. Sloshing ions put perpendicular pressure anisotropy at turning points, so instability drive weakens towards the mirror cell's centre. A small plasma column radius with respect to the ion Larmor radius also aids stability (Tsidulko & Chernoshtanov 2014). And, AIC is suppressed if the mirror's axial length is shorter than a critical length (Tajima *et al.* 1977; Tajima & Mima 1980; Nicks *et al.* 2023),

$$L_{\mathrm{c}} = 2\pi^2 \sqrt{\frac{T_{i\parallel}}{\beta_\perp T_{i\perp}}} \left(\frac{c}{\omega_{\mathrm{pi}}}\right). \tag{4.8}$$

The critical length $L_{\mathrm{c}} \approx 182\,\mathrm{cm}$ is very close to WHAM's length $2L_{\mathrm{p}} = 196\,\mathrm{cm}$, again taking $\beta_\perp = 0.17$ and assuming $c/\omega_{\mathrm{pi}} = 5.9\,\mathrm{cm}$ for density $n = 3 \times 10^{13}\,\mathrm{cm}^{-3}$ at sloshing-ion turning points. Third, DCLC simply has a faster growth rate and decreases plasma beta before AIC can be triggered.

To summarize: AIC with low axial mode number may be marginally unstable for WHAM, based on the highest possible $\beta_\perp$ and density n at sloshing-ion turning points. But multiple effects weaken AIC drive and so may explain why it does not appear in our simulations.

4.5. *Comparison with real mirrors*

In real mirror devices, discrete DCLC modes can persist stably for $\sim\mathcal{O}(1\,\mathrm{ms})$ (Shmigelsky *et al.* 2024), but DCLC can also appear as discrete bursts of enhanced fluctuations with duration ~10 to 100 μs (Coensgen *et al.* 1975; Yamaguchi 1996; Shmigelsky *et al.* 2024). Our simulations do not show bursting, nor did previous simulations by Cohen *et al.* (1983). Yamaguchi (1996) explained bursting DCLC in the GAMMA-6A experiment using a quasilinear model with bounce-averaged electron Landau damping; they appealed to (i) separation between DCLC scattering and axial outflow time scales (i.e. $1/\nu_{\perp\perp} \ll \tau_{\mathrm{GD}}$); and (ii) fast time variation in DCLC growth rate with slower variation in electron-Landau damping rate. In our simulations, $1/\nu_{\perp\perp} \sim \tau_{\mathrm{GD}}$ at order of magnitude (figure 8*b*); DCLC appears marginally stable and does not damp upon ions within a time scale $\ll \tau_{\mathrm{GD}}$. It would be interesting to see if future kinetic simulations with longer simulation durations, electron-Landau damping or other physical effects can replicate DCLC bursting.

Both TMX-U and GDT saw that DCLC could be driven at sloshing-ion turning points instead of at the mirror midplane $z = 0$ (Berzins & Casper 1987; Shmigelsky *et al.* 2024). Why does DCLC have strongest drive at $z = 0$, versus at the turning points, in our simulations of WHAM? In TMX-U, the end-plug could be stabilized on one side and not the other due to a combination of axial flows from the central cell and localized ECH at the end-plug outer-turning point (Berzins & Casper 1987). As for GDT versus WHAM, we cannot answer definitively, but we note that WHAM's shorter axial length of 2 m may constrain DCLC's axial eigenmodes as compared with GDT's 7 m length.

Where do cool ions come from in real experiments? In WHAM, DCLC-scattered ions escape with large $|v_\parallel|$ and are not trapped. Charge exchange between beam ions and cool neutrals can generate $< 1\,\mathrm{keV}$ ions that trap in the midplane's electrostatic potential well; prerequisite cool neutrals naturally outgas from plasma-facing materials. In tandem mirrors like TMX-U, central-cell outflow into end-plug cells can also provide cool ions to stabilize DCLC (Simonen *et al.* 1983; Berzins & Casper 1987). Central-cell outflow may also help to reduce the growth rate of curvature-driven collisionless trapped-particle modes (Rosenbluth 1982; Berk *et al.* 1983), as outflowing

https://doi.org/10.1017/S0022377825000480 Published online by Cambridge University Press

ions can sample good curvature near mirror throats and help to couple adjacent MHD-unstable and stable mirror cells.

Cool-ion stabilization of DCLC may face problems in larger and more powerful mirrors. The axial electrostatic well at $z = 0$, which traps cool ions, will become shallower due to ion–ion pitch-angle scattering of the beam ions. Pitch-angle scattering is counter-balanced by neutral-beam capture via charge exchange (CX) or impact ionization, as both processes create new hot ions with 45° pitch-angle. The CX between hot ions / fast neutrals also pumps out the isotropized, scattered hot ions, so one CX event collimates the ions' pitch-angle distribution more effectively than one impact-ionization event. But, the CX cross-section drops relative to impact ionization for beam energies $\gtrsim 70$ keV (Endrizzi *et al.* 2023, figure 10). It thus becomes harder to collimate the ion pitch-angle distribution and harder to maintain an axial electrostatic potential well with $\mathcal{O}(10^2)$ keV NBI (e.g. Forest *et al.* 2024, figure 6). And, tandem central-cell outflow reduces fusion performance and may set limits on power-plant reactor design (e.g. Frank *et al.* 2025, § 3.2). Future mirror designs may thus need other methods to help stabilize DCLC.

The WHAM experiment began operating in July 2024 (Anderson *et al.* 2024). A comparison between experimental data and our simulations is not yet available. We anticipate that WHAM plasmas and diagnostics may be tuned to create and measure DCLC modes in future experimental campaigns.

5. Conclusions

We have performed 3-D kinetic-ion simulations of WHAM, initialized with a neutral-beam-injected deuteron population with $T_i \sim 10$ keV and cool, isothermal-fluid electrons with $T_e \sim 1$ keV, to assess kinetic plasma stability in a high-performance, collisionless-ion regime. We find that WHAM's beam-ion distribution is unstable to an electrostatic, flute-like ($k \approx k_\perp$) mode that grows on $\lesssim 1$ μs time scales; it propagates azimuthally around the column in the ion diamagnetic direction and has angular frequency between Ω_{i0} and $2\Omega_{i0}$. We identify it as the DCLC mode, well known from prior mirror experiments (Coensgen *et al.* 1975) and previously anticipated to be a possible concern for WHAM (Endrizzi *et al.* 2023).

The plasma column and DCLC fluctuations settle into a steady-state decay by $t = 6$ μs. Particles escape axially with confinement time $\tau_p = n/(\mathrm{d}n/\mathrm{d}t) \sim 10^2$ μs in a 'gas dynamic' regime, wherein the scattering rate into the loss cone equals or exceeds the rate of free-streaming axial loss from the mirror. Particle losses are due to collisionless $v_\perp$ scattering upon the DCLC modes; the particle–wave correlation time is approximately ${\Omega_{i0}}^{-1}$ at the mirror midplane. Particle losses and velocity-space diffusion are strongest at the plasma's radial edge, whereas the plasma column's core can maintain $\mathrm{d}F/\mathrm{d}v_\perp > 0$ at low $v_\perp$.

We review well known and experimentally tested methods for stabilizing DCLC: addition of cool plasma to fill the loss cone, larger plasma extent (smaller gradient) and parallel electron kinetics including Landau damping. In 3-D simulations with cool ions initialized at the plasma's radial edge, the beam ions' confinement time can be raised by up to 9×, though an order-unity ratio of cool/hot ion number density is needed and the cool-ion confinement is poorer than that of the beam ions. The best-case beam-ion confinement time of several 100 μs also remains two orders of magnitude below the ideal, 'classical' confinement time of 0.1–0.2 s. In a real experiment, the cool ions must be provided and replenished by external sources because DCLC does not scatter beam ions into the axial electrostatic potential well

https://doi.org/10.1017/S0022377825000480 Published online by Cambridge University Press

(Kesner 1973, 1980) where they could be trapped to help stabilize DCLC. The DCLC-scattered beam ions are lost because they retain large parallel speeds and so never enter the trapped region of phase space.

Our simulations are limited, especially in the electric field model and isothermal-fluid electron closure. Future work may incorporate electron inertia, an electron energy equation, drift-kinetic electrons or more to help model (i) bounce-averaged electron Landau damping, and (ii) the plasma's axial and radial electric potential structure, which dictate outflows and rotation. And, the initial condition of a hot, beam-ion plasma with only mild slowing-down upon electrons is idealized. A two-way coupling between Hybrid-VPIC and CQL3D-m over a 20 ms laboratory shot duration, passing DCLC quasilinear diffusion coefficients from kinetic simulations into the Fokker–Planck equation, may yield more realistic predictions. Adding neutral-ion interactions to our CQL3D-m models would improve our cool-ion stabilization modelling. Other subsystems on WHAM are not modelled, for example heating of ions and electrons via radio-frequency and microwave radiation, respectively, or biased end-rings within the expanders used to drive rotation and shear flow. So, future work may also consider a wider range of fuelling and heating scenarios in WHAM and next-step mirror devices.

Supplementary material

The supplementary material for this article can be found at https://doi.org/10.1017/S0022377825000480

Acknowledgements

Conversations with D. Bindl, S. Dettrick, M. Francisquez, R. Groenewald, M. Koepke, D. Ryutov, D. Sutherland, D. Yakovlev, M. Yu and the entire WHAM team are gratefully acknowledged. We also thank the anonymous referees for constructive comments that have improved this paper.

Editor Peter Catto thanks the referees for their advice in evaluating this article.

Funding

Funding for this work was provided by Realta Fusion, the U.S. Department of Energy (DOE), and the U.S. National Science Foundation (NSF). WHAM collaboration work is supported by the U.S. DOE through ARPA-E DE-AR0001258, Commonwealth Fusion Systems, Realta Fusion, Wisconsin Alumni Research Foundation and a lengthy list of collaborators providing valuable equipment. AT was partly supported by NSF PHY-2010189 and the DOE Fusion Energy Sciences Postdoctoral Research Program, administered by the Oak Ridge Institute for Science and Education (ORISE) and Oak Ridge Associated Universities (ORAU) under DOE contract DE-SC0014664.

High-performance computing resources were provided by the National Energy Research Scientific Computing Center (NERSC), a DOE Office of Science User Facility, via allocation FES-ERCAP0026655; Anvil at Purdue University's Rosen Center for Advanced Computing (McCartney *et al.* 2014; Song *et al.* 2022) via allocation PHY230179 from the NSF Advanced Cyberinfrastructure Coordination Ecosystem: Services & Support (ACCESS) program; Amazon Web Services' Compute for Climate Fellowship awarded to Realta Fusion; Los Alamos Institutional Computing; and UW–Madison's Center for High

Throughput Computing (Center for High Throughput Computing, 2006). ACCESS (Boerner *et al.* 2023) is supported by NSF grants #2138259, #2138286, #2138307, #2137603 and #2138296.

All opinions expressed in this paper are the authors' and do not necessarily reflect the policies and views of DOE, ORAU or ORISE.

Declaration of interests

C.B.F. is a co-founder of Realta Fusion; D.A.E., S.J.F. and J.V. are employees of Realta Fusion. This work was partly supported by a grant from Realta Fusion to the University of Wisconsin–Madison.

REFERENCES

AAMODT, R.E. 1977 Electron stabilization of drift-cone modes. *Phys. Fluids* **20** (6), 960–962.

AAMODT, R.E., COHEN, B.I., LEE, Y.C., LIU, C.S., NICHOLSON, D.R. & ROSENBLUTH, M.N. 1981 Nonlinear evolution of drift cyclotron modes. *Phys. Fluids* **24** (1), 55–65.

AAMODT, R.E., LEE, Y.C., LIU, C.S. & ROSENBLUTH, M.N. 1977 Nonlinear dynamics of drift-cyclotron instability. *Phys. Rev. Lett.* **39** (26), 1660–1663.

ANDERSON, J.K., *et al.* 2024 First physics results from the wisconsin hts axisymmetric mirror (wham). In Bulletin of the American Physical Society, 66th Annual Meeting of the APS Division of Plasma Physics, Abstract ZI03.00001. American Physical Society. https://meetings.aps.org/Meeting/DPP24/Session/ZI03.1

BAGRYANSKY, P.A. 2024 Progress of open systems at budker institute of nuclear physics. *J. Plasma Phys.* **90** (2), 905900218.

BAJBORODOV, J.T., IOFFE, M.S., KANAEV, B.I., SOBOLEV, R.I. & JUSHMANOV, E.E. 1971 Investigation of Plasma Decay in the PR-6 Adiabatic Trap. In Proceedings of the Fourth International Conference on Plasma Physics and Controlled Nuclear Fusion Research, vol. **2**. International Atomic Energy Agency.

BALDWIN, D.E. 1977 End-loss processes from mirror machines. *Rev. Mod. Phys.* **49** (2), 317–339.

BALDWIN, D.E., BERK, H.L. & PEARLSTEIN, L.D. 1976 Turbulent lifetimes in mirror machines. *Phys. Rev. Lett.* **36** (17), 1051–1054.

BEKLEMISHEV, A.D., BAGRYANSKY, P.A., CHASCHIN, M.S. & SOLDATKINA, E.I. 2010 Vortex confinement of plasmas in symmetric mirror traps. *Fusion Sci. Technol.* **57** (4), 351–360.

BERK, H.L., ROSENBLUTH, M.N., WONG, H.V., ANTONSEN, T.M. & BALDWIN, D.E. 1983 Fast growing trapped-particle modes in tandem mirrors. *Soviet J. Plasma Phys.* **9** (1), 108.

BERK, H.L. & STEWART, J.J. 1977 Quasi-linear transport model for mirror machines. *Phys. Fluids* **20** (7), 1080–1088.

BERS, A. & GRUBER, S. 1965 Negative-energy plasma waves and instabilities at cyclotron harmonics. *Appl. Phys. Lett.* **6** (2), 27–28.

BERZINS, L.V. & CASPER, T.A. 1987 Ion microinstability at the outer sloshing-ion turning point of the tandem mirror experiment upgrade (TMX-U). *Phys. Rev. Lett.* **59** (13), 1428–1431.

BOERNER, T.J., DEEMS, S., FURLANI, T.R., KNUTH, S.L. & TOWNS, J. 2023 Access: advancing innovation: nsf's advanced cyberinfrastructure coordination ecosystem: services & support. In *Practice and Experience in Advanced Research Computing, PEARC '23*, pp. 173–176. Association for Computing Machinery.

BOWERS, K.J., ALBRIGHT, B.J., YIN, L., BERGEN, B. & KWAN, T.J.T. 2008 Ultrahigh performance three-dimensional electromagnetic relativistic kinetic plasma simulationa). *Phys. Plasmas* **15** (5), 055703.

BURKHART, G.R., GUZDAR, P.N. & KOEPKE, M.E. 1989 Theoretical modeling of drift cyclotron loss-cone instability mode structures. *Phys. Fluids B* **1** (3), 570–580.

Center for High Throughput Computing 2006 Center for High Throughput Computing. https://doi.org/10.21231/GNT1-HW21

CHAUDHRY, M.B. 1983 Electrostatic drift ion cyclotron waves in sheet plasmas with and without ambipolar field. *J. Phys. Soc. Japan* **52** (3), 856–866.

COENSGEN, F.H., CUMMINS, W.F., LOGAN, B.G., MOLVIK, A.W., NEXSEN, W.E., SIMONEN, T.C., STALLARD, B.W. & TURNER, W.C. 1975 Stabilization of a neutral-beam-sustained, mirror-confined plasma. *Phys. Rev. Lett.* **35** (22), 1501–1503.

COHEN, B.I. & MARON, N. 1980 Simulation of drift-cone modes. *Phys. Fluids* **23** (5), 974–980.

COHEN, B.I., MARON, N. & NEVINS, W.M. 1984 Simulation of drift-cyclotron-loss-cone modes in tandem mirrors with sloshing ions. *Phys. Fluids* **27** (3), 642–649.

COHEN, B.I., MARON, N. & SMITH, G.R. 1982 Some nonlinear properties of drift-cyclotron modes. *Phys. Fluids* **25** (5), 821–841.

COHEN, B.I., SMITH, G.R., MARON, N. & NEVINS, W.M. 1983 Particle simulations of ion-cyclotron turbulence in a mirror plasma. *Phys. Fluids* **26** (7), 1851–1865.

CORRELL, D.L., CLAUSER, J.H., COENSGEN, F.H., CUMMINS, W.F., DRAKE, R.P., FOOTE, J.H., FUTCH, A.H., GOODMAN, R.K., GRUBB, D.P. & MELIN, G.M. 1980 Production of large-radius, high-beta, confined mirror plasmas. *Nucl. Fusion* **20** (6), 655–664.

DRAKE, R.P., CASPER, T.A., CLAUSER, J.F., COENSGEN, F.H., CORRELL, D.L., CUMMINS, W.F., DAVIS, J.C., FOOTE, J.H., FUTCH, A.H. & GOODMAN, R.K. 1981 The effect of end-cell stability on the confinement of the central-cell plasma in TMX. *Nucl. Fusion* **27** (3), 359–364.

ELWASIF, W.R., BERNHOLDT, D.E., SHET, A.G., FOLEY, S.S., BRAMLEY, R., BATCHELOR, D.B. & BERRY, L.A. 2010 The design and implementation of the swim integrated plasma simulator. In Proceedings of the 18th Euromicro Conference on Parallel, Distributed and Network-based Processing. (ed. D. MARCO, J.BOURGEOIS & T. GROSS), pp. 419–427. IEEE, Computer Society Press.

ENDRIZZI, D., *et al.* 2023 Physics basis for the Wisconsin HTS axisymmetric mirror (WHAM). *J. Plasma Phys.* **89** (5), 975890501.

FERRARO, R.D., LITTLEJOHN, R.G., SANUKI, H. & FRIED, B.D. 1987 Nonlocal effects on the drift cyclotron loss cone dispersion relation in cylindrical geometry. *Phys. Fluids* **30** (4), 1115–1122.

FERRON, J.R. & WONG, A.Y. 1984 The dependence of the drift cyclotron loss cone instability on the radial density gradient. *Phys. Fluids* **27** (5), 1287–1300.

FOREST, C.B., *et al.* 2024 Prospects for a high-field, compact break even axisymmetric mirror (BEAM) and applications. *J. Plasma Phys.* **90** (1), 975900101.

FOWLER, T.K., MOIR, R.W. & SIMONEN, T.C. 2017 A new simpler way to obtain high fusion power gain in tandem mirrors. *Nucl. Fusion* **57** (5), 056014.

FRANK, S.J., *et al.* 2025 Confinement performance predictions for a high field axisymmetric tandem mirror. Accepted in *J. Plasma Phys*.

GARY, S.P., MCKEAN, M.E., WINSKE, D., ANDERSON, B.J., DENTON, R.E. & FUSELIER, S.A. 1994 The proton cyclotron instability and the anisotropy/β inverse correlation. *J. Geophys. Res.* **99** (A4), 5903–5914.

GERVER, M.J. 1976 Stabilization of drift cyclotron loss cone instability with additions of small amounts of cool plasma. *Phys. Fluids* **19** (10), 1581–1590.

GURNETT, D.A. & BHATTACHARJEE, A. 2017 *Introduction to Plasma Physics*. Second edn. Cambridge University Press.

HARRIS, E.G. 1959 Unstable plasma oscillations in a magnetic field. *Phys. Rev. Lett.* **2** (2), 34–36.

HASEGAWA, A. 1978 Stabilization of drift-cyclotron loss-cone mode by low-frequency density fluctuations. *Phys. Rev. Lett.* **40** (14), 938–941.

HELLINGER, P., TRÁVNÍČEK, P., KASPER, J.C. & LAZARUS, A.J. 2006 Solar wind proton temperature anisotropy: linear theory and WIND/SWE observations. *Geophys. Res. Lett.* **33**, L09101.

ICHIMURA, M., INUTAKE, M., KATSUMATA, R., HINO, N., HOJO, H., ISHII, K., TAMANO, T. & MIYOSHI, S. 1993 Relaxation of pressure anisotropy due to Alfvén-ion-cyclotron fluctuations observed in ion-cyclotron-range-of-frequency-heated mirror plasmas. *Phys. Rev. Lett.* **70** (18), 2734–2737.

IOFFE, M.S., KANAEV, B.I., PASTUKHOV, V.P. & YUSHMANOV, E.E. 1975 Stabilization of cone instability of collisional plasma in a mirror trap. *Soviet J. Exp. Theor. Phys.* **40** (6), 1064–1069.

ISENBERG, P.A., MARUCA, B.A. & KASPER, J.C. 2013 Self-consistent ion cyclotron anisotropy-beta relation for solar wind protons. *Astrophys. J.* **773** (2), 164.

IVANOV, A.A. & PRIKHODKO, V.V. 2017 Gas dynamic trap: experimental results and future prospects. *Physics Uspekhi* **60** (5), 509–533.

KADOMTSEV, B.B., MIKHAILOVSKII, A.B. & TIMOFEEV, A.V. 1964 Negative energy waves in dispersive media. *Sov. Phys. JETP* **20** (6), 1517.

KANAEV, B.I. 1979 Stabilization of drift loss-cone instability (DCI) by addition of cold ions. *Nucl. Fusion* **19** (3), 347–359.

KATSUMATA, R., ICHIMURA, M., INUTAKE, M., HOJO, H., MASE, A. & TAMANO, T. 1996 Eigenmode excitation of Alfvén ion cyclotron instability. *Phys. Plasmas* **3** (12), 4489–4495.

KENNEL, C.F. & PETSCHEK, H.E. 1966 Limit on stably trapped particle fluxes. *J. Geophys. Res.* **71** (1), 1–28.

KESNER, J. 1973 Inverse ambipolar potential in a magnetic mirror configuration. *Plasma Phys.* **15** (6), 577–584.

KESNER, J. 1980 Axisymmetric sloshing-ion tandem-mirror plugs. *Nucl. Fusion* **20** (5), 557–562.

KOEPKE, M., ELLIS, R.F., MAJESKI, R.P. & MCCARRICK, M.J. 1986*a* Experimental observation of bounce-resonance Landau damping in an axisymmetric mirror plasma. *Phys. Rev. Lett.* **56** (12), 1256–1259.

KOEPKE, M., MCCARRICK, M.J., MAJESKI, R.P. & ELLIS, R.F. 1986*b* Three-dimensional mode structure of the drift cyclotron loss-cone instability in a mirror trap. *Phys. Fluids* **29** (10), 3439–3444.

KOEPKE, M.E. 1992 Effects of bounce-resonance damping on the harmonics of a plasma microinstability. *Phy. Fluids B* **4** (5), 1193–1198.

KOTELNIKOV, I.A. 2025 On the stability of the $m = 1$ rigid ballooning mode in a mirror trap with high-beta sloshing ions. *J. Plasma Phys.* **91** (2), E54. https://doi.org/10.1017/S0022377824001338

KOTELNIKOV, I.A. & CHERNOSHTANOV, I.S. 2018 Isotopic effect in microstability of electrostatic oscillations in magnetic mirror traps. *Phys. Plasmas* **25** (8), 082501.

KOTELNIKOV, I.A., CHERNOSHTANOV, I.S. & PRIKHODKO, V.V. 2017 Electrostatic instabilities in a mirror trap revisited. *Phys. Plasmas* **24** (12), 122512.

LE, A., STANIER, A., YIN, L., WETHERTON, B., KEENAN, B. & ALBRIGHT, B. 2023 Hybrid-VPIC: an open-source kinetic/fluid hybrid particle-in-cell code. *Phys. Plasmas* **30** (6), 2305–05600.

LINDGREN, N.E., BIRDSALL, C.K. & LANGDON, A.B. 1976 Electrostatic waves in an inhomogeneous collisionless plasma. *Phys. Fluids* **19** (7), 1026–1034.

MCCARRICK, M.J., BOOSKE, J.H. & ELLIS, R.F. 1987 Observations of the dependence of unstable drift cyclotron loss cone mode characteristics on plasma density. *Phys. Fluids* **30** (2), 614–617.

MCCARTNEY, G., HACKER, T. & YANG, B. 2014 Empowering faculty: a campus cyberinfrastructure strategy for research communities. *Educause Rev.* https://er.educause.edu/articles/2014/7/empowering-faculty-a-campus-cyberinfrastructure-strategy-for-research-communities

MIKHAILOVSKII, A.B. & TIMOFEEV, A.V. 1963 Theory of cyclotron instability in a non-uniform plasma. *Sov. Phys. JETP* **17** (3), 626.

MYER, R.C. & SIMON, A. 1980 Nonlinear saturation of the drift cyclotron loss-cone instability. *Phys. Fluids* **23** (5), 963–973.

NICKS, B.S., PUTVINSKI, S. & TAJIMA, T. 2023 Stabilization of the Alfvén-ion cyclotron instability through short plasmas: fully kinetic simulations in a high-beta regime. *Phys. Plasmas* **30** (10), 102108.

PETERSON, E.E. 2019 A laboratory model for magnetized stellar winds. PhD thesis, University of Wisconsin–Madison.

PETROV, Y.V. & HARVEY, R.W. 2016 A fully-neoclassical finite-orbit-width version of the CQL3D Fokker–Planck code. *Plasma Phys. Control. Fusion* **58** (11), 115001.

PITERSKIĬ, V.V., YUSHMANOV, E.E. & YAKOVETS, A.N. 1995 Stabilization of the drift-cone instability by a flow shear. *Soviet J. Exp. Theor. Phys. Lett.* **62**, 303.

POST, R.F. 1987 The magnetic mirror approach to fusion. *Nucl. Fusion* **27** (10), 1579–1739.

POST, R.F. & ROSENBLUTH, M.N. 1966 Electrostatic instabilities in finite mirror-confined plasmas. *Phys. Fluids* **9** (4), 730–749.

PRIKHODKO, V.V., *et al.* 2018 Stability and Confinement Studies in the Gas Dynamic Trap. In 27th IAEA Fusion Energy Conference, IAEA-CN-258/EX/P5-25. International Atomic Energy Agency. https://conferences.iaea.org/event/151/contributions/6261

QIAN, T., ANDERSON, J.K., ENDRIZZI, D., FOREST, C.B., PIZZO, J.D., SANWALKA, K., YAKOVLEV, D., YU, M. & ZARNSTORFF, M.C. 2023 Experimental Plans for MHD Stability in WHAM. In Bulletin of the American Physical Society, 65th Annual Meeting of the APS Division of Plasma Physics, Abstract UP11.00077. American Physical Society. https://meetings.aps.org/Meeting/DPP23/Session/UP11.77

ROBERTS, K.V. & TAYLOR, J.B. 1962 Magnetohydrodynamic equations for finite larmor radius. *Phys. Rev. Lett.* **8** (5), 197–198.

ROSE, D.V., GENONI, T.C., WELCH, D.R., MEHLHORN, T.A., PORTER, J.L. & DITMIRE, T. 2006 Flute instability growth on a magnetized plasma column. *Phys. Plasmas* **13** (9), 092507.

ROSENBLUTH, M.N. 1982 Topics in plasma instabilities: trapped-particle modes and MHD. *Phys. Scr.* **2A**, 104–109.

ROSENBLUTH, M.N., KRALL, N.A. & ROSTOKER, N. 1962 Finite Larmor radius stabilization of "Weakly" unstable confined plasmas. *Nuclear Fusion: 1962 Supplement, Part 1,* **10** (170), 143–150.

RYUTOV, D.D., BERK, H.L., COHEN, B.I., MOLVIK, A.W. & SIMONEN, T.C. 2011 Magneto-hydrodynamically stable axisymmetric mirrors. *Phys. Plasmas* **18** (9), 092301.

SANUKI, H. & FERRARO, R.D. 1986 Nonlocal theory of DCLC modes in a plasma slab with an ambipolar field. *Phys. Scripta* **34** (1), 58–62.

SHMIGELSKY, E.A., MEYSTER, A.K., CHERNOSHTANOV, I.S., LIZUNOV, A.A., SOLOMAKHIN, A.L. & YAKOVLEV, D.V. 2024 Kinetic instabilities in two-isotopic plasma in the GDT magnetic mirror. *J. Plasma Phys.* **90** (6), 905900605.

SIMONEN, T., *et al.* 2008 The axisymmetric tandem mirror: a magnetic mirror concept game changer magnet mirror status study group. Tech. Rep. LLNL-TR-408176. Lawrence Livermore National Laboratory.

SIMONEN, T.C., *et al.* 1983 Operation of the tandem-mirror plasma experiment with skew neutral-beam injection. *Phys. Rev. Lett.* **50** (21), 1668–1671.

SONG, X.C., *et al.* 2022 Anvil - system architecture and experiences from deployment and early user operations. In *Practice and Experience in Advanced Research Computing 2022: Revolutionary: Computing, Connections, You, PEARC '22*. Computing, Association for Computing Machinery.

STANIER, A., CHACÓN, L. & CHEN, G. 2019 A fully implicit, conservative, non-linear, electromagnetic hybrid particle-ion/fluid-electron algorithm. *J. Comput. Phys.* **376**, 597–616.

STIX, T.H. 1992 *Waves in Plasmas*. American Institute of Physics.

TAJIMA, T. & MIMA, K. 1980 Stabilization of the Alfvén-ion cyclotron instability in inhomogeneous media. *Phys. Fluids* **23** (3), 577–589.

TAJIMA, T., MIMA, K. & DAWSON, J.M. 1977 Alfvén ion-cyclotron instability: its physical mechanism and observation in computer simulation. *Phys. Rev. Lett.* **39** (4), 201–204.

TANG, W.M., PEARLSTEIN, L.D. & BERK, H.L. 1972 Finite Beta stabilization of the drift-cone instability. *Phys. Fluids* **15** (6), 1153–1155.

TSIDULKO, Y.A. & CHERNOSHTANOV, I.S. 2014 Alfvén ion-cyclotron instability in an axisymmetric trap with oblique injection of fast atoms. *Plasma Phys. Rep.* **40** (12), 955–964.

WATSON, G.N. 1922 *A Treatise On the Theory of Bessel Functions*. Cambridge University Press.

WETHERTON, B.A., LE, A., EGEDAL, J., FOREST, C., DAUGHTON, W., STANIER, A. & BOLDYREV, S. 2021 A drift kinetic model for the expander region of a magnetic mirror. *Phys. Plasmas* **28** (4), 2105–01572.

YAKOVLEV, D.V., SHALASHOV, A.G., GOSPODCHIKOV, E.D., MAXIMOV, V.V., PRIKHODKO, V.V., SAVKIN, V.Y., SOLDATKINA, E.I., SOLOMAKHIN, A.L. & BAGRYANSKY, P.A. 2018 Stable confinement of high-electron-temperature plasmas in the GDT experiment. *Nucl. Fusion* **58** (9), 094001.

YAMAGUCHI, H. 1996 Amplitude oscillation of an instability in a plasma in the presence of a damping mechanism. *J. Phys. Soc. Japan* **65** (10), 3115–3118.

YERGER, E.L., KUNZ, M.W., BOTT, A.F.A. & SPITKOVSKY, A. 2025 Collisionless conduction in a high-beta plasma: a collision operator for whistler turbulence. *J. Plasma Phys.* **91** (1), E20.

YOSHIKAWA, M., *et al.* 2019 Suppression of flute-like fluctuation by potential formation in GAMMA 10/PDX. *Nucl. Fusion* **59** (7), 076031.

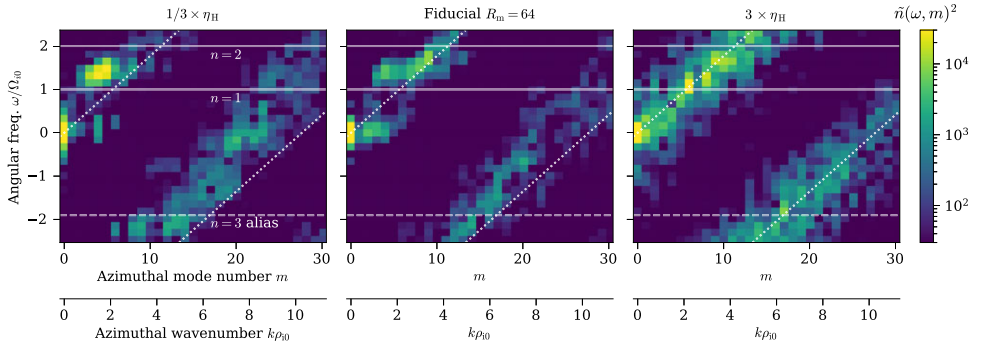

FIGURE 14. Effect of hyper-resistivity, increasing (*a*) to (*c*), upon density-fluctuation Fourier spectra in WHAM $R_m = 64$ simulations; panel (*b*) is the same data as figure 6(*c*). Fourier spectra and annotations constructed like in figure 6, at same $r = 2.69\rho_{i0}$ over $t = 3$ to 6 τ_{bounce}, but the colourmap range and 2-D plot domain/range are changed.

Appendix A. Hyper-resistivity scan

Hyper-resistivity, although intended to suppress gridscale numerical noise, may also alter DCLC mode structure as discussed in § 2.2. Figure 14 shows that raising or decreasing η_H by a factor of 3 alters the spectrum of density fluctuations at the plasma edge; with higher η_H, the spectrum broadens and is less coherent.

Appendix B. Electron parallel response

To obtain the electrons' parallel response in § 4.3, we start again from Stix (1992, § 14-3, (9)), neglecting spatial derivatives of order $\partial^2 g/\partial y^2$ or higher in Stix's notation, where g is the guiding-centre distribution. For a Maxwellian guiding-centre distribution, the susceptibility is

$$\chi_s = \left(\frac{\omega_{ps}}{\Omega_s}\right)^2 \sum_{n=-\infty}^{\infty} e^{-\lambda} I_n(\lambda) \left\{ \left(\frac{k_\perp}{k}\right)^2 \left[\frac{2n}{k_\perp^2}\left(1 - \frac{n\epsilon}{k_\perp}\right) + \frac{\epsilon}{k_\perp}\right] \frac{Z(\zeta_n)}{k_\parallel} + \left(\frac{k_\parallel}{k}\right)^2 \frac{2}{k_\parallel^2}\left(1 - \frac{n\epsilon}{k_\perp}\right)[1 + \zeta_n Z(\zeta_n)] \right\}, \tag{B1}$$

where the modified Bessel function $I_n(\lambda)$ has argument $\lambda = k_\perp^2/2$, the plasma dispersion function $Z(\zeta_n)$ has argument $\zeta_n = (\omega - n)/k_\parallel$ and the variables $\omega, \epsilon, k, k_\perp, k_\parallel$ are all dimensionless following the same species-specific scheme used for (3.3). Equation (B1) is valid for any $\boldsymbol{k}$ angle. The limit $\zeta_n \to \infty$ and $k_\parallel/k \to 0$ recovers the perpendicular susceptibility given by (3.3). The limit $\epsilon/k_\perp \to 0$ recovers the standard Harris (1959) dispersion relation (Gurnett & Bhattacharjee 2017, § 10.2).

Let us simplify (B1). Take the limits $\lambda \to 0$ and $\zeta_{\pm 1} = (\omega \mp 1)/k_\parallel \approx \mp 1/k_\parallel \to \infty$ in order to expand $e^{-\lambda} I_n(\lambda)$ and $Z(\zeta_{\pm 1})$. But, make no assumptions on the magnitude of $\zeta_0 = \omega/k_\parallel$. Also, drop all $|n| > 1$ Bessel terms. The result is

$$\chi_s = \left(\frac{\omega_{ps}}{\Omega_s}\right)^2 \left\{ \left(\frac{k_\perp}{k}\right)^2 \left[\frac{\epsilon}{k_\perp \omega} - 1\right] \zeta_0 Z(\zeta_0) + \left(\frac{k_\parallel}{k}\right)^2 \frac{2}{k_\parallel^2}[1 + \zeta_0 Z(\zeta_0)] \right\}, \tag{B2}$$

https://doi.org/10.1017/S0022377825000480 Published online by Cambridge University Press

which yields (4.4) after putting in dimensions. The limit $\zeta_0 \to \infty$ recovers the familiar cold-fluid result, written as follows in dimensional variables:

$$\chi_s = \left(\frac{k_\perp}{k}\right)^2 \frac{\omega_{ps}^2}{\Omega_s^2}\left[1 - \frac{\epsilon\Omega_s}{k_\perp \omega}\right] - \left(\frac{k_\parallel}{k}\right)^2 \frac{\omega_{ps}^2}{\omega^2}. \tag{B3}$$

A subtlety appears when expanding (B1) into (B2). Consider the susceptibility tensor components $\chi_{\perp\perp}$ and $\chi_{\parallel\parallel}$ for a hot homogeneous plasma (Stix 1992, § 10). The perpendicular response simplifies in the cold-fluid limit,

$$\chi_{\perp\perp} \to \frac{\omega_{ps}^2}{\Omega_s^2}. \tag{B4}$$

But, $\chi_{\perp\perp}$ is cancelled by the analogous expansion of $\chi_{\parallel\parallel}$ when (i) both $k_\perp$ and $k_\parallel$ are finite; (ii) ζ_0 is kept finite; and (iii) terms of order $\mathcal{O}(\lambda^1)$ are kept in expanding $e^{-\lambda} I_0(\lambda)$. The said expansion gives

$$\begin{aligned}\chi_{\parallel\parallel} &\to \frac{\omega_{ps}^2}{\Omega_s^2}\frac{2}{k_\parallel^2}\left[1 + \zeta_0 Z(\zeta_0)\right]\left(1 - \lambda + \mathcal{O}(\lambda^2)\right) \\ &= \frac{\omega_{ps}^2}{\Omega_s^2}\left\{\frac{2}{k_\parallel^2}\left[1 + \zeta_0 Z(\zeta_0)\right] - \frac{k_\perp^2}{k_\parallel^2} - \frac{k_\perp^2}{k_\parallel^2}\zeta_0 Z(\zeta_0)\right\},\end{aligned} \tag{B5}$$

with $k_\parallel$ dimensionless as before. Then, in the combined electrostatic susceptibility

$$\chi \approx (k_\perp/k)^2 \chi_{\perp\perp} + (k_\parallel/k)^2 \chi_{\parallel\parallel} + (2k_\parallel k_\perp/k^2)\chi_{\perp\parallel}, \tag{B6}$$

we see that (B4) and (B5) partly cancel, and only a parallel contribution $-(k_\perp/k)^2(\omega_{ps}/\Omega_s)^2\zeta_0 Z(\zeta_0)$ remains. This remainder term can be seen in (B2). When the $\zeta_0 \to \infty$ limit is taken, it is this parallel remainder that provides the usual perpendicular response $\chi_{\perp\perp} \to \omega_{ps}^2/\Omega_s^2$. This is to some extent a semantic quibble; we can also say that the remainder term $-(k_\perp/k)^2(\omega_{ps}/\Omega_s)^2\zeta_0 Z(\zeta_0)$ cancels the parallel term $-(k_\perp/k)^2(\omega_{ps}/\Omega_s)^2$ to leave only the perpendicular term $+(k_\perp/k)^2(\omega_{ps}/\Omega_s)^2$ in (B6). But, the overall point stands that the perpendicular term in (B2) can be significantly modified by the parallel response, even when $k_\parallel \ll k_\perp$; the regulating parameter is ζ_0.

https://doi.org/10.1017/S0022377825000480 Published online by Cambridge University Press